Journal of Fusion Energy (2025) 44:22
https://doi.org/10.1007/s10894-025-00492-5

RESEARCH

Liquid Metal Droplet Ejection Through Bubble Formation Under Hydrogen Plasma and Radical Exposure

J. G. A. Scholte[1,2] · R. S. Al[2] · D. Horsely[3] · M. Iafrati[4] · A. Manhard[5] · E. Martelli[4] · M. Morbey[2] · S. Roccella[4] · J. W. M. Vernimmen[2] · T. W. Morgan[1,2]

Accepted: 6 March 2025 / Published online: 29 March 2025

Abstract

Liquid tin constrained in a capillary porous structure could be an alternative plasma-facing component to tungsten for the divertor of a future magnetic confinement fusion reactor. However, due to the hydrogen–tin interaction droplets can be ejected, which is a potential showstopper due to an increased radiation in the plasma core. This has been recently observed in experiments in the ASDEX Upgrade tokamak. In this work, the theory of droplet ejection is reviewed, both theoretically and experimentally and potential solutions are tested in nano-PSI, a low flux unmagnetized plasma device. Droplet ejection was demonstrated via shadowgraphy observations to be driven by bubble formation and bursting followed by jetting. The generality of droplet ejection was verified by exposing liquid lithium, sodium, potassium, gallium, indium, tin, lead, and bismuth to hydrogen plasma in nano-PSI. Furthermore, the influence of the capillary structure was tested, by exposing multiple CPS targets. Ejection of droplets was observed for all post-transition metals and with all targets. Moreover, it was shown that free radicals alone are sufficient for droplet ejection, rather than plasma ions. Further, we predict and observe that the droplet ejection is suppressed by increasing the temperature above a critical value for a given radical flux. Our analysis shows that droplet production is highly challenging to prevent under expected fusion reactor conditions. Since droplet ejection cannot be prevented, the approach of using tin as a liquid metal plasma-facing material requires revision.

Keywords Liquid metal · Divertor · Tin · Supersaturation · Droplets

Introduction

The most mature concept for a plasma-facing component for the divertor of a fusion reactor uses solid tungsten (W) monoblocks bonded to a copper alloy heat sink [1]. The divertor has to withstand the highest heat and particle flux in both tokamaks and stellerators. Therefore, tungsten has been chosen due to its high melting temperature, heat conductivity, and resistance to erosion [2]. However, there will still be erosion and material degradation; therefore, the divertor is expected to be replaced every 1.5 full power years in DEMO, decreasing the effective operational time [1]. Replacing solid W with liquid tin (Sn) could extend the divertor's lifespan, particularly in high heat flux areas, offering a promising solution for DEMO. A liquid is not affected by neutrons, is more resilient to transient heat loads due to vapour shielding [3], and allows for easier replacement of eroded material. In this concept, called a liquid metal divertor (LMD), Sn is typically confined in a W capillary porous structure (CPS) to prevent MHD instabilities from ejecting liquid metal from the surface into the plasma. Two different conceptual designs using a CPS have been proposed for an LMD with Sn, both of which would require minimal change to in vessel components compared to the current EU-DEMO design [4, 5].

A growing number of experiments have demonstrated that droplets are ejected from Sn under hydrogen plasma

✉ J. G. A. Scholte
j.g.a.scholte@tue.nl

1 Eindhoven University of Technology, De Zaale, 5612AZ Eindhoven, The Netherlands

2 DIFFER-Dutch Institute for Fundamental Energy Research, De Zaale 20, 5612 AJ Eindhoven, The Netherlands

3 UKAEA, Culham Science Centre, Abingdon, Oxon OX14 3DB, UK

4 ENEA Frascati Research Center, Via Enrico Fermi 45, 00044 Frascati, RM, Italy

5 Max-Planck-Institut für Plasmaphysik, Boltzmannstraße 2, 85748 Garching, Germany

exposure, even in many cases when a CPS is employed [6–10]. These could lead to unacceptable radiative losses in a fusion device upon reaching the core, as recently observed in ASDEX-Upgrade [11]. A proposed explanation is that hydrogen ions and radicals dissolve in the Sn until the saturation limit is reached [6]. At this point, the liquid is super saturated and a bubble can nucleate and grow until it finally collapses, ejecting Sn in the process.

This paper presents investigations of the generality of the droplet production phenomenon, and determination of the operational space for the prevention of droplet formation. From theory, it will be deduced in section "The Theory of Droplet Ejection from Liquid Metals When Exposed to a Hydrogen Plasma" that all liquid metals (LMs) that do not chemically react with hydrogen can form gas bubbles and eject droplets. Two sets of experiments are carried out using the nano-PSI plasma device, and their methodology is described in section "Experimental Methodology". The bubbling and droplet ejection phenomenon is examined using a camera and by analysing nearby witness plates with Rutherford Backscattering Spectroscopy (RBS). This was done with the following post-transition metals: gallium, indium, tin, lead, and bismuth. These are not all suitable for an LMD, but they can provide useful insight into the generality of this phenomenon. These results are shown in section "Results and Discussion". Furthermore, droplet ejection size and rate was previously found to be reduced with the reduction in CPS pore size [6, 8]. Therefore, different CPS concept designs were also exposed to hydrogen plasmas in nano-PSI, to determine which is the most resistant to droplet ejection. These results are also shown in section "Results and Discussion". In section "What Do These Results Mean for a Liquid Metal Divertor?" we examine the implications of our observed findings for application in future fusion reactors and describe what mitigation approaches are viable.

The Theory of Droplet Ejection from Liquid Metals When Exposed to a Hydrogen Plasma

Instabilities That Lead to the Use of a CPS

Liquid metals have been proposed since the 1970s as an alternative to solid tungsten as a PFC [12]. The challenge of using a liquid metal as a PFC is to ensure that it remains securely in place, preventing it from entering the plasma. In the tokamak DIII-D, a 1 mm thick Lithium (Li) foil with a diameter of 25.4 mm was exposed to divertor hydrogen plasma conditions. From this free surface layer (FSL) on the probe-head surface Li was ejected, eventually causing a radiative collapse [13]. In the HT-7 tokamak, Li droplets have been ejected during various experiments with a flowing liquid limiter, also resulting in plasma disruptions [14]. During both experiments, the loss of Li was attributed to Rayleigh-Taylor (RT) instabilities due to $\vec{j} \times \vec{B}$ forces. Whilst exposing W to ITER-like Edge Localized Modes (ELMs) in the plasma gun facility quasistationary plasma accelerator (QSPA-T) droplets would be ejected from the target, which was attributed to a Kelvin-Helmholtz (KH) instability [15, 16]. To mitigate these instabilities, capillary porous structures (CPS) were proposed [17]. The adhesion forces between the structure and the liquid create a capillary pressure to keep the liquid in place. This pressure can be determined using the Young-Laplace equation:

$$p = \frac{2\gamma \cos\theta}{r} \tag{1}$$

With γ the surface tension, θ the contact angle between the liquid and the solid, and r the pore radius. Jaworski et al. [18] obtained a critical current density, above which perpetuations caused by $\vec{j} \times \vec{B}$ are RT unstable.

$$j_{crit} = \frac{1}{B}\left(\frac{4\pi^2}{\lambda^2}\gamma + \rho g\right) \tag{2}$$

Here B is the magnetic field, g is the gravitational acceleration, ρ the mass density, and λ the wavelength of the perturbation. Therefore, this instability can be suppressed by having a CPS with $r < \lambda$ such that $j < j_{crit}$. Miloshevskii et al. [19] determined that the maximum velocity difference between plasma and liquid to stabilize against the KH instability is:

$$\Delta V_{crit} = \sqrt{\frac{\rho_{\mathrm{LM}} + \rho_{\mathrm{p}}}{\rho_{\mathrm{LM}}\rho_{\mathrm{p}}}\left(\frac{g(\rho_{\mathrm{LM}} - \rho_{\mathrm{p}})}{k} + \gamma k + \frac{B^2}{2\pi\mu}\right)} \tag{3}$$

with wave number $k = 2\pi/\lambda$, magnetic permeability μ and subscript LM and p referring to the properties of the LM and the plasma respectively. Using a reasoning similar to that before, this instability can be suppressed by having a CPS with $r < \lambda$ such that $\Delta V < \Delta V_{crit}$. A radius $< 100\,\mu$m is sufficient for both Li and Sn to stabilize against the predicted current densities and velocity differences during ELMs in ITER [18, 20].

Overview of Recent Studies

Several papers related to the ejection of LMs in a hydrogen plasma, even during the use of CPS or in cases where droplets should otherwise be suppressed, have been published in the past years. An overview of these papers is also given in Table 1. In Ou et al. [6] who used nano-PSI and Magnum-PSI to expose an FSL and a CPS, both with Sn to a hydrogen plasma, they observed that a CPS

Table 1 Overview of droplet ejection in liquid metals or gas bubbles in solid metals in recent papers

Paper	Plasma device	n_e [10^{16} m^{-3}]	T_e [eV]	Γ_i [10^{14} cm^{-2} s^{-1}]	Metal	Container
Ou et al. [6]	Nano-PSI | Magnum-PSI	-|-	0.1-1| < 5	$\sim 10-100$ | 10^5	Sn (l)	FSL & Mo CPS mesh
Manhard et al. [7, 9]	ECR (PlaQ)	–	25	120	Sn (s,l)	FSL (s,l) & sintered CPS (s,l)
Hamana et al. [21]	Inductively coupled	1.5–2.5	15–215	0.2–7.1	Ga(l)	FSL
Tamura et al. [23]	Inductively coupled	1.2–3.9	~ 3	~ 100	SBLE (l)	FSL
Shefer et al. [24]	ECR	~ 1	~ 5	–	Sn(s), Pb(s) and PbO	FSL

Magnum-PSI and nano-PSI both have a cascaded arc source. In this table, ECR stands for Electron cyclotron resonance. In the metals and container columns, an (s) refers to solid and (l) to liquid metal

reduced the number and size of droplets. Furthermore, they noticed that reducing the pore size of a CPS reduces the number of droplets, but it was not possible to fully suppress them. Manhard et al. [7, 9] exposed both an FSL and a CPS with Sn to a low-temperature D plasma in the ECR plasma source "PlaQ". The erosion of Sn increased by 3 orders of magnitude by going from a temperature just below to just above the melting point. The erosion could be significantly reduced when using a CPS compared to using an FSL of Sn, but was still substantially higher than that of solid Sn. After exposure, Sn droplets larger than the typical pore size were observed on the crucible around the CPS. In Hamana et al. [21] liquid gallium (Ga) was used and with a quadrupole mass spectrometer (QMS) it was determined that an incubation time was required before droplet ejection started, in their case it was 18–35 s. In that study, an increase in the ejection frequency was noted with the increase in the LM temperature and ion flux, whilst a reduction was observed with an increase in ion energy. Tin-bismuth-lithium-erbium (Sn:42.1% Bi:30.8% Li:24.9% Er:2.2% or SBLE), which is considered a blanket concept [22] was exposed to a hydrogen plasma by Tamura et al. [23]. This material started to form large gas bubbles and ejected LM into the plasma. When a bubble collapsed, an increase in the partial hydrogen pressure was measured using a differentially pumped quadrupole mass analyzer (QMA). From this, they were able to determine that $\approx 38\%$ of the ion flux ended up in gas bubbles. This phenomenon is not exclusive to liquids, but can also occur on solid Sn, as shown by Shefer et al. [24] and Manhard et al. [7]. In that work, Sn dust particles were exposed to a hydrogen plasma. After 7 h a FIB cut was made in which gas bubbles were observed in the metal. It should be mentioned that droplet ejection is not always observed. When an Sn-filled limiter was exposed in the tokamak FTU, the ejection of droplets was not observed. An Sn core fraction $n_{Sn}/n_e \approx 5 \times 10^{-4}$ was obtained from the measured effective atomic number (Z_{eff}), which could be explained by evaporation and sputtering [25].

Lithium seems less affected than Sn, and droplet ejection is rarely mentioned [26–28]. During exposure of LiSn and Li in the divertor of the tokamak COMPASS [29], no droplet ejection was observed until the CPS damaged at $17-18$ MWm^{-2}. Additionally, when Li was exposed in the limiter of the tokamak EAST, no droplets were observed [30]. When described, it can be associated with the $\vec{j} \times \vec{B}$ forces mentioned previously [13, 14, 18, 31].

Possible Explanations for Droplet Ejection Under Hydrogen Exposure

We identify five possible explanations given in literature that could describe this phenomenon. Assuming that the reason for the formation of gas bubbles and the ejection of liquid particles is the same in all the above-mentioned papers. Here, we review those explanations and determine which one is universally applicable.

1. *Localized boiling due to the high heat flux from the plasma:* This is a common phenomenon in welding where an LM is also in contact with a plasma, that is usually referred to as spatter [32]. However, if this were the case one would expect lithium (Li) to cause more droplet ejection than Sn, since Li has a higher vapour pressure. Furthermore, the vapour pressure of the LMs was always negligible at the operational temperature of the discussed papers. The temperature of Sn was just 10 °C above the melting point in Manhard et al. [9] for example.
2. *Lorentz's force due to the scrape-off layer current and the oblique incidence magnetic field:* This was concluded to be the cause of the Li splash from the divertor of DIII-D, which caused a radiative collapse [13]. This was possible, since the lithium was not confined by a CPS. A CPS with a pore size < 1mm should have been able to suppress the $\vec{j} \times \vec{B}$ forces [18], see Eq. (2). Even for the FSL experiments this cannot be an appropriate

explanation since the there was no magnetic field whilst there was droplet ejection in some cases [6, 7, 9, 21, 23].

3. *Kelvin-Helmholtz instability due to a flow speed difference between the interface of the plasma and the LM:* This could form waves on the LM surfaces, eventually leading to droplet ejection [19]. However, high flow velocities ($> 8\,\mathrm{kms}^{-1}$) are required for this instability to occur, even for a FSL of Sn [20] whilst in nano-PSI, the sound speed is $< 5\,\mathrm{kms}^{-1}$. Even when expanding Eq. (3) to include the viscosity of the plasma [33], a CPS could stabilize against the sound speed in nano-PSI.
4. *The formation of a volatile component between the metal and hydrogen:* An example is given below for the formation of stannane gas.

$$\mathrm{Sn} + 4\mathrm{H}^{\cdot} \longrightarrow \mathrm{SnH_4(g)} \tag{4}$$

The volatile component could erode the surface and decompose on a hot surface in accordance to:

$$\mathrm{SnH_4(g)} \longrightarrow \mathrm{Sn} + 2\mathrm{H_2(g)} \tag{5}$$

In the case of SnH_4, decomposition can occur at room temperature [34]. This could explain why there was Sn erosion at all for solid Sn [7], even though there should not be any evaporation or sputtering. However, the formation of volatile components is a surface effect and thus cannot explain the ejection of droplets. For this to happen, they need to be formed inside the Sn, or diffuse into the Sn before decomposing following Eq. (5). However, stannane is highly unstable [34], thus this process seems unlikely. For these reasons, we can dismiss this as a universal explanation.

5. *The formation of* H_2 *gas within the LM after surpassing the solubility limit in the metal:* When a hydrogen plasma contacts a surface, part of the hydrogen will be implanted in the material. In a liquid, when the concentration of the solute hydrogen exceeds the saturation limit, gas bubbles can nucleate within the liquid. This bubble can grow until it finally burst at the surface. Gas bubbles can even form in solid metal [7, 24, 35]. However, for a bubble in a solid to burst the pressure needs to surpass the yield strength rather than the surface tension, which is orders of magnitude higher. Elements such as alkali metals readily form hydride compounds with hydrogen, leading to solid precipitates that act as a continuous sink for hydrogen until the liquid is fully converted. This would explain why droplet formation is not observed in Li. For other liquid metals which do not readily form solid compounds with hydrogen, this offers a universal source for bubble formation. Therefore, this option is further explored below.

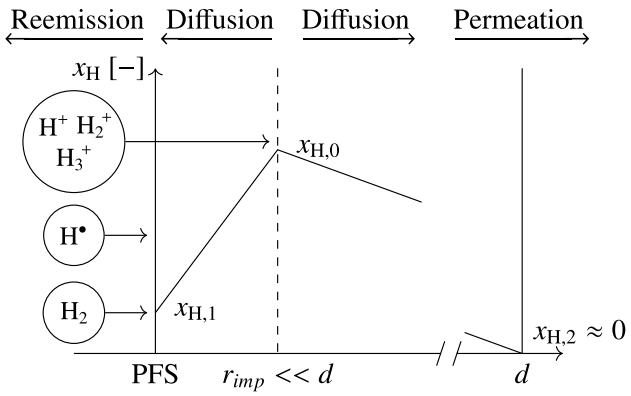

Fig. 1 A schematic overview of the hydrogen permeation model in an LM during steady-state, based on [36]. The y-axis represents the dissolved hydrogen mole fraction. Radicals and gas are adsorbed at the plasma-facing surface (PFS), and are therefore the main contribution to the hydrogen mole fraction at the PFS. On the other hand, the ions have sufficient energy to be implanted inside the material and are here all assumed to be deposited at the characteristic implantation depth (r_{imp}). The x-axis is a representation of the depth of the LM layer and is not to scale. The total thickness of the liquid metal is d

Enhanced Solubility in Liquid Metals

To understand this phenomenon, one first needs to know how much hydrogen is dissolved in the liquid. During this derivation, the equations will be kept general, such that it is applicable for all LMs. In Fig. 1, a schematic overview of hydrogen permeation in LMs in steady state is shown. There are three locations marked: the implantation depth of the ions (r_{imp}, subscript 0), the plasma-facing surface (PFS, subscript 1), and the total depth of the liquid (d, subscript 2). At the PFS, the hydrogen dissolved in the metal and the hydrogen in the plasma are in thermodynamic equilibrium.

Molecular Hydrogen

To determine the hydrogen fraction (x_H) in the LM, let us initially examine the scenario involving pure molecular hydrogen gas in contact with an LM. This interaction could be represented using the following reaction equation:

$$\frac{1}{2}\mathrm{H_2(g)} \rightleftharpoons \mathrm{H(sln)} \tag{6}$$

Here, solution (sln) indicates that hydrogen is dissolved in a liquid metal. The steady-state hydrogen molar fraction in a liquid exposed to hydrogen gas can be calculated using Sievert's law:

$$x_{\mathrm{H},g} = \frac{\text{Moles of H}}{\text{Total moles}} = K_{\mathrm{H},g}\sqrt{\frac{p_{\mathrm{H_2}}{}^{\circ}}{p}} \tag{7}$$

In this equation, it is assumed that H_2 is an ideal gas, with $p_{\mathrm{H_2}}$ the partial pressure of hydrogen gas, p° the pressure at standard conditions ($T = 0\,°\mathrm{C}$ and $P = 1$ bar) and $K_{\mathrm{H},g}$, a temperature-dependent constant, which can be obtained using:

$$K_{\mathrm{H},g} = \exp\left(-\frac{\Delta G^{\circ}_{\mathrm{H_2}}}{R_g T}\right) \tag{8}$$

Here R_g is the ideal gas constant, T [K] the temperature and $\Delta G^{\circ}_{\mathrm{H_2}}$ [J mol^{-1}] the Gibbs free energy at standard conditions of the chemical reaction in Eq. (6), which can generally be written as:

$$\Delta G^{\circ}_{\mathrm{H_2}} = \Delta G^{\circ}_f\left(\mathrm{H}_{(\mathrm{LM})}\right) - \frac{1}{2}\Delta G^{\circ}_f\left(\mathrm{H_2(g)}\right) = \Delta H^{\circ} - \Delta S^{\circ} T \tag{9}$$

With ΔH° and ΔS° the change in the standard enthalpy and entropy of hydrogen solution in the LM and ΔG°_f the standard Gibbs free energy of formation. Some relevant values are given in Table 5 and the resulting $x_{\mathrm{H},g}$ for various metals at ambient pressure is shown in Fig. 2. From this graph, it can be concluded that the solubility of hydrogen in Sn is exceptionally low compared to that of other LMs.

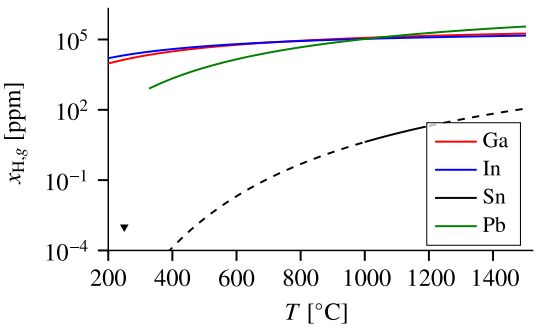

Fig. 2 Hydrogen equilibrium mole fraction, in ppm, for selected metals at ambient pressure. The black solid and dashed graph is the data and extrapolated data from Bever and Floe [37], whilst the downwards pointing triangle indicate the maximum Sn mole fraction at the melting point from Nemanič et al. [38]. The data for In and Ga are taken from [39] whilst for Pb [40] was used, $\Delta G^{\circ}_{\mathrm{H2}}$ is also given in Table 5. The plot shows that the solubility of Sn is about four orders of magnitude lower than the other LMs, within the confirmed data regime

Free Hydrogen Radicals

We can further expand the solubility model by adding free radicals to the gas. A kinetic reaction-diffusion model has been developed by Pick et al. [41], which has been extended to study hydrogen retention in solid tungsten [42–44]. This requires the cross-section of direct abstraction (σ_{exc}) and the activation energy for adsorption(E_A), desorption (E_D) and resurfacing (E_R). For Sn, E_A was estimated to be 0.73 eV from a fit through experimental data [45]. This matched the value of 0.80 eV calculated for a surface covered by SnH [46]. However, the other values are, to our the best of our knowledge, not given in the literature. Therefore, in this work the approach proposed by Ou et al. [6] will be used instead. Here an equilibrium is assumed between the radicals and the hydrogen dissolved in the liquid metal, similar to the gas. This can be expressed as follows:

$$\mathrm{H}\cdot \rightleftharpoons \mathrm{H(sln)} \tag{10}$$

The main assumption of this approach is that dissolved hydrogen can form a free radical once released. Whilst it is more probable that it will be released as molecular hydrogen, as in Eq. (6). Therefore, the contribution of the hydrogen radicals will most likely be overestimated, by assuming that Eq. (10) is the only contribution in the release of hydrogen from the liquid metal. When assuming that the equilibrium reaction exists in Eq. (10) exists, Henry's law can be used to calculate the equilibrium molar fraction using:

$$x_{\mathrm{H},r} = \beta K_{\mathrm{H},r}\frac{p_{\mathrm{H}}}{p^{\circ}} \tag{11}$$

An additional β factor is introduced, when $\beta = 1$ no correction to Henry's law is used, setting $\beta < 1$ compensates for the overestimation of this approach. The radical partial pressure (p_{H}) is not always known, and the Hertz-Knudsen equation can be used to relate it to the radical flux.

$$p_{\mathrm{H}} = \Gamma_{\mathrm{H}}\sqrt{2\pi m_{\mathrm{H}} k_B T} \tag{12}$$

With m_{H} the mass of a hydrogen atom and k_B Boltzmann's constant. The equilibrium constant from Eq. (11) is given by:

$$K_{\mathrm{H},r} = \exp\left(-\frac{\Delta G^{\circ}_{\mathrm{H}}}{R_g T}\right) \tag{13}$$

With ΔG°_H the Gibbs free energy at standard conditions of the chemical reaction in Eq. (10).

$$\Delta G^{\circ}_{\mathrm{H}} = \Delta G^{\circ}_f\left(\mathrm{H}_{(\mathrm{LM})}\right) - \Delta G^{\circ}_f(\mathrm{H}\cdot) \tag{14}$$

This value is generally not empirically known, due to a lack of experimental data. However, it can be calculated by combining Eqs. (9) and (14) into:

$$\Delta G^{\circ}_{\mathrm{H}} = \Delta G^{\circ}_{\mathrm{H_2}} + \frac{1}{2}\Delta G^{\circ}_{f}\left(\mathrm{H_2}(g)\right) - \Delta G^{\circ}_{f}(\mathrm{H^-}) \tag{15}$$

For $\Delta G^{\circ}_{\mathrm{H_2}}$ the experimental relation in Eq. (9) together with the parameters in Table 5 can be used. The standard Gibbs free energy of formation can generally be written as:

$$\Delta G^{\circ}_{f} = \Delta H^{\circ}_{f} - T\Delta S^{\circ} \tag{16}$$

With ΔH°_{f} the standard enthalpy of formation. From [47] we find that $\Delta H^{\circ}_{f}(\mathrm{H_2(g)}) = 0\,\mathrm{J\,mol^{-1}}$, $S^{\circ}(\mathrm{H2(g)}) = 130.68\,\mathrm{J\,K^{-1}\,mol^{-1}}$, $\Delta H^{\circ}_{f}(\mathrm{H^-}) = 217.998\ \mathrm{kJ\,mol^{-1}}$, and $S^{\circ}(\mathrm{H^-}) = 114.717\,\mathrm{J\,K^{-1}\,mol^{-1}}$. Filling in these numbers gives the following.

$$K_{\mathrm{H},r} = \exp\left(\frac{217998 - 49.37T}{R_g T}\right) K_{\mathrm{H},g} \tag{17}$$

This additional prefactor to $K_{\mathrm{H},g}$ indicates that radicals have much more influence on the equilibrium fraction than the molecules. To obtain $x_{\mathrm{H},1}$ at the PFS, it is assumed that the contribution of molecules and radicals can be added together.

$$x_{\mathrm{H},\,1} = x_{\mathrm{H},g} + x_{\mathrm{H},r} \tag{18}$$

This is most likely to be an overestimation, but we will see in Sect. 2.7 that this does not have such a big influence on the end result.

Hydrogen Ions

The third and last form of hydrogen are the ions ($\mathrm{H^+}$, $\mathrm{H_2}^+$ and $\mathrm{H_3}^+$). These are directly implanted in the liquid surface at r_{imp}, which depends on the kinetic ion energy and the LM pecies. Afterwards, hydrogen will diffuse away from the implantation zone according to Fick's law. The diffusion flux J [$\mathrm{mol\,m^{-2}\,s^{-1}}$] can be calculated using:

$$J = \frac{D\rho}{M}\nabla x_{\mathrm{H}} \tag{19}$$

In this equation, D is the diffusivity constant of hydrogen through the LM, M the molar mass and ∇x_{H} the gradient in molar concentration between the implantation zone and the PFS. This aligns with the hydrogen permeation model, assuming that diffusion is the rate-limiting step rather than recombination or desorption [36]. As a result, the diffusion and implantation flux counterbalance each other ($J = -\Gamma_{imp}$), see Fig. 1. This equation can, therefore, be rewritten to find the molar concentration of hydrogen in the implantation zone:

$$x_{\mathrm{H},0} \leq x_{\mathrm{H},\,1} + \frac{\Gamma_{imp} r_{imp} M}{N_A D \rho} \tag{20}$$

Here, the Avogadro constant (N_A) is introduced to convert between moles and molecules. This equation gives a maximum for $x_{\mathrm{H},0}$ since there is also a diffusion of hydrogen towards d. This is still a reasonable estimation since $r_{imp} << d$. The implanted ion flux can be calculated using:

$$\Gamma_{imp} = (1 - R)\Gamma_i \tag{21}$$

Where R is the reflection coefficient of the incident hydrogen ions. The hydrogen ion flux (Γ_i) can be calculated using:

$$\Gamma_i = 0.5 n_e \sqrt{\frac{k_B T_e + \gamma k_B T_i}{m_i}} \tag{22}$$

with γ the heat capacity ratio, not to be confused with the surface tension, and m_i is the mass of the ions. Furthermore, it is assumed that the electron and ion temperature are equal ($T_e = T_i$), when the plasma is generated in a cascaded arc source [48]. The only remaining unknowns that cannot be measured are r_{imp} and R, which can be determined using a binary collision code such as SDTrimSP [49] or SRIM [50].

Supersaturation Ratio

A convenient measure to use is the saturation ratio, which indicates how close we are to thermochemical equilibrium. This is defined as follows:

$$\alpha \equiv \frac{x_{\mathrm{H}}}{x_{\mathrm{H},g}} \tag{23}$$

with x_{H} the hydrogen molar fraction in the LM, i.e. due to the gas, ions and radicals. Another convenient measure is the supersaturation ratio:

$$S \equiv \frac{x_{\mathrm{H}}}{x_{\mathrm{H},g}} - 1 = \alpha - 1 \tag{24}$$

Here, α is the ratio between the dissolved gas in a liquid and the thermodynamic equilibrium, and S gives the factor by which you exceed this value. When $\alpha > 1$ or $S > 0$ a fluid is called supersaturated. A common example in daily life is the solubility of CO_2 in champagne ($S \approx 4$) [51, 52], or sodas ($S \approx 2{-}3$) [53]. We can now rewrite Eq. (24) using Eq. (11) and (20) as follows:

$$S = \exp\left(-\frac{217998 - 49.37T}{R_g T}\right)\frac{\beta p_{\mathrm{H}}}{\sqrt{p_{\mathrm{H_2}} p^{\circ}}} + \frac{\Gamma_{imp} r_{imp} M \sqrt{p^{\circ}}}{N_A D \rho K_{\mathrm{H},g} \sqrt{p_{\mathrm{H_2}}}} \tag{25}$$

We note that this is still generally written and is applicable to all plasma devices.

Nucleation: The Formation of a Gas Bubble

When considering an LM in an environment with just H_2 gas $\alpha = 1$ and $S = 0$ because the solute hydrogen is in equilibrium with the H_2 gas. When considering the influence of ions and radicals $\alpha > 1$ and $S > 0$, the metal will always become supersaturated in the presence of ions and radicals. As with champagne or sodas, this may provide a driving force for bubble nucleation. The pressure inside this bubble can be calculated using the Laplace pressure:

$$p = p_0 + \frac{2\gamma}{r} \tag{26}$$

Here p_0 is the gas pressure above the liquid. Additionally, we can use Sievert's law (Eq. (7)) to relate the mole fraction ration to the gas pressure ratio of two different states.

$$\frac{x_{\mathrm{H},crit}}{x_{\mathrm{H},g}} = \sqrt{\frac{p_{crit}}{p_{\mathrm{H}_2}}} \tag{27}$$

with $x_{\mathrm{H},crit}$ and p_{crit} the critical mole fraction and pressure respectively. Here, critical refers to the state where the pressure in the bubble is just higher than the pressure that can be sustained by surface tension. Combining Eqs. (23), (26) and (27) gives a critical bubble radius.

$$r_{crit} = \frac{2\gamma}{p_{\mathrm{H}_2}(\alpha^2 - 1)} \tag{28}$$

If a bubble remains smaller than r_{crit}, the pressure in the bubble is less than the surface tension, and thus it will shrink. If the bubble is larger than r_{crit} it can grow, through diffusion by gas in the surrounding liquid into the bubble. In this equation, it is assumed that $p_{\mathrm{H}_2} = p_0$, since a boundary layer of hydrogen gas would form just above the liquid that is in equilibrium [52]. Note that if $p_{\mathrm{H}_2} < p_0$, r_{crit} would be lower than the value given in Eq. (28). There are four ways in which this initial bubble with $r_b > r_{crit}$ can nucleate, which are described in [54, 55]:

Type I Classical homogeneous nucleation: This can occur spontaneously, without the presence of a gas pocket or surface within the liquid. For this reason, it typically needs a high supersaturation ratio $S > 100$ to materialize.

Type II Classical heterogeneous nucleation: Catalysed by another metal or impurity in the liquid.

Type III Pseudo-classical nucleation: This occurs in a pre-existing gas cavity, for example, a scratch or pore where $r < r_{crit}$.

Type IV Non-classical nucleation: This occurs in a pre-existing gas cavity, for example, a scratch or pore where $r > r_{crit}$.

The structure of a CPS resembles a cellulose fibre, which allows bubble nucleation of CO_2 in champagne [52]. Or the more famous example of Mentos in soda, where the cavities in the candy allow non-classical nucleation [56]. Therefore, even when the supersaturation in the LM is relatively low ($S < 5$), bubble nucleation can be expected due to the presence of trapped gas bubbles or irregularities in the CPS. Further, in a FSL, there will still be expected to be small scratches at the walls where bubbles can nucleate. Therefore, we can expect bubbles to form at latest if $S \approx 5$.

Droplet Ejection

Figure 3 shows a schematic representation of the collapse of a gas bubble leading to droplet ejection. Once a bubble with $r_b > r_{crit}$ has nucleated, it will rise toward the surface, due to the buoyancy force because the density in the gas is lower than in the liquid. This growth is limited by the diffusivity of hydrogen through the LM, which typically increases with temperature [51, 52]. Therefore, the bubble size and the bubbling frequency increase with increasing temperature. The growth and rise of a bubble continues until only a small liquid film remains on top of the gas bubble. As soon as this film is breached, small droplets called film droplets can be formed, depending on the liquid [57]. There is now a deformation in the liquid surface, and the surface tension forces will act to restore the surface equilibrium which minimizes the surface area. The momentum of this inward collapse is

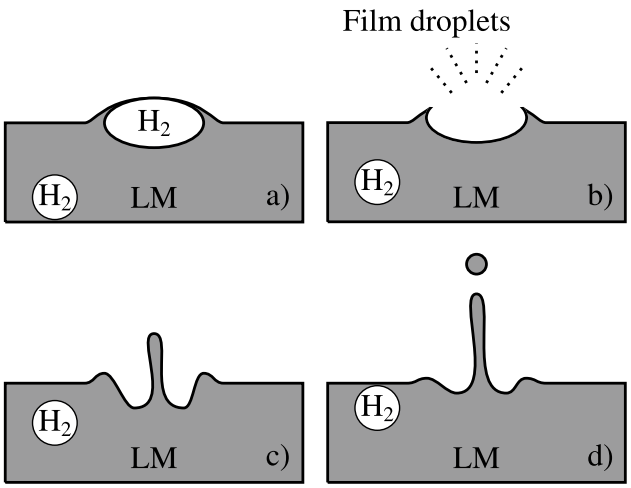

Fig. 3 Schematic representation of the collapse of a gas bubble leading to droplet ejection. **a** A gas bubble has risen to the top of the LM. **b** The liquid film on top of the bubble is breached, and small droplets are ejected. **c** The pit left by the gas bubble is filled with LM and a jet is formed. **d** The jet stretches and thinness, until a droplet is ejected

redirected vertically, creating a high-speed gush of liquid that shoots upward, forming a Worthington jet [58]. As the jet moves upward, it becomes thinner until the liquid breaks into smaller droplets because of surface tension, which minimizes the surface area due to the Rayleigh-Plateau instability. The radius of the gas bubble influences the radius of the ejected liquid droplet (r_d), where an empirical relation has been obtained $r_d \propto r_b^{1.2}$ [57]. By substituting the Young-Laplace pressure Eq. (1) in the ideal gas law and assuming that the total number of dissolved hydrogen molecules is independent of the gas bubble size in which they accumulate, we find:

$$m_{loss} \propto r_b^{8/5} \tag{29}$$

Therefore, the total mass loss can be efficiently reduced by restricting the size of bubbles using a CPS, as has also been experimentally shown [6, 8]. Furthermore, it has been suggested that jet formation could even be suppressed if the gas bubble remains small enough i.e. by reducing the pore radius [59]. To find this bubble radius, the dimensionless Ohnesorge number (Oh) is first defined as the ratio of viscous forces to the combined effect of inertial and surface tension.

$$\mathrm{Oh} = \frac{\mu}{\sqrt{\rho \gamma r_b}} \tag{30}$$

For high Oh, viscous forces dominate and if $\mathrm{Oh} > \mathrm{Oh}^*$ they are sufficient to suppress the formation of jets. Lee et al. [59] experimentally obtained a critical value of $\mathrm{Oh}^* = 0.052 \pm 0.005$. This allows us to calculate a critical radius r_b^* below which bubble collapse does not cause droplet ejection. Depending on the material and temperature this gives a value $r_b = 30\,\mathrm{nm} - 1\,\mu\mathrm{m}$, see also Fig. 4. Although both r_{crit} and r_b^* are called the critical bubble radius, they differ in that if $r_b < r_{crit}$, a bubble shrinks due to surface tension and therefore does not collapse, whilst if $r_b < r_b^*$ it grows and collapses, but a jet is not formed. Therefore, a gas bubble (or rather a CPS) should have a radius below r_{crit} or r_b^* to suppress droplet ejection.

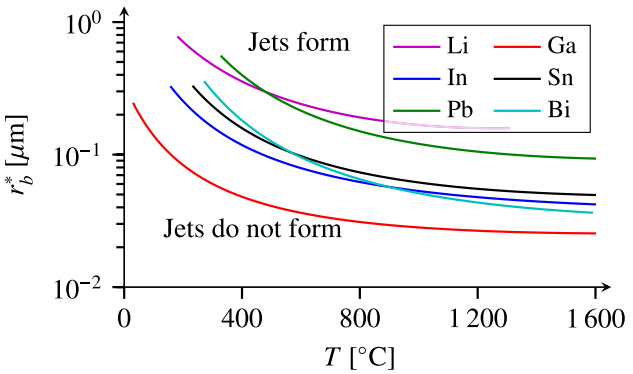

Fig. 4 Critical bubble radius below which jets do not form when a gas bubble collapses

Summary and Implication of the Theory

In Figs. 5 and 6a the supersaturation ratio is shown for liquid metals in contact with hydrogen gas and radicals or ions, respectively, by setting the first or second term in Eq. (25) to zero. If $S < 100$ classical homogeneous nucleation cannot occur and bubbles need to nucleate on surfactants, impurities, or pre-existing gas cavities ($S = 5$). Both are indicated with a green dashed line. However, in a CPS type I nucleation is likely not a limiting factor, since the pores can act as gas cavities or irregularities in the tungsten surface can form during manufacturing. It might result in a difference in the bubbling frequency between different CPSs. If $S > 100$, classical homogeneous nucleation can occur and the difference between various CPS should be minimized in terms of bubbling frequency. Additionally, Figs. 5 and 6b shows the critical bubble radius (r_{crit}) for Sn. This latter value is material dependent since it depends on γ; however, this value does not change more than a factor of 2 for the materials of interest; see also Table 5. In these graphs, a green horizontal dotted line is added at $r_{crit} = 1\,\mu\mathrm{m}$, since this is approximately the minimum pore size limit of a CPS based on existing technology [8]. If we are in a regime below this line, it is currently not possible to make a CPS with a pore radius smaller than the critical bubble radius. Hence, when a hydrogen gas bubble nucleates in the liquid, it can grow and eject droplets. If we are in a regime above this line, it is stable since the pore size prevents gas bubbles from reaching the critical radius. Note also that $r^* < 1\,\mu\mathrm{m}$ for all considered metals at all relevant temperatures, see Fig. 4, and thus it seems impossible to manufacture a CPS with $r < r^*$.

Data for the hydrogen composition for various plasma devices are noted in Table 2. From Fig. 5 it can be concluded that it is only possible to suppress droplet ejection in a radical environment by either going to a very

Table 2 Estimates of the partial hydrogen atom and gas pressure and ion flux in various relevant plasma devices

	Nano-PSI [60]	Magnum-PSI [61]	ITER [62, 63]	DEMO [64]
Γ_i [at m^{-2} s^{-1}]	$\sim 10^{20}$	10^{23}–10^{25}	$\sim 5 \times 10^{23}$	10^{23}–10^{25}
p_{H} [Pa]	~ 1	0.1–0.5	1–10	1–100
p_{H_2} [Pa]	~ 50	0.1–0.5	1–10	1–100

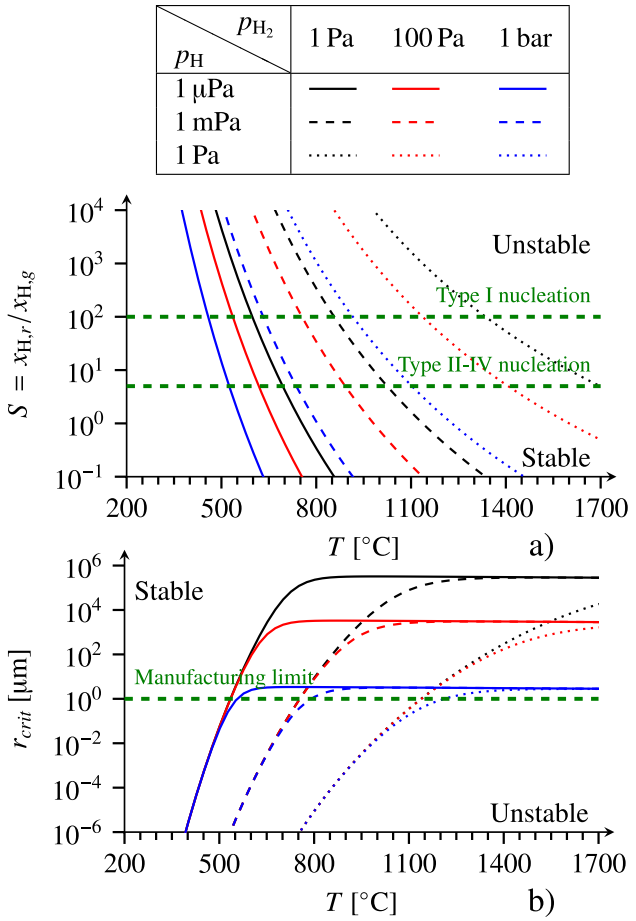

Fig. 5 **a** The hydrogen supersaturation ratio in any LM in steady state due to gas and radicals, whilst neglecting ions (**b**) and the critical bubble radius associated with this for Sn for $\beta = 1$. This later is material dependent, since it depends on γ. It shows that p_H should either be kept low or the temperature high to prevent droplet ejection. However, in the divertor $p_H > 1$ Pa and thus a surface temperature is required where evaporation becomes significant

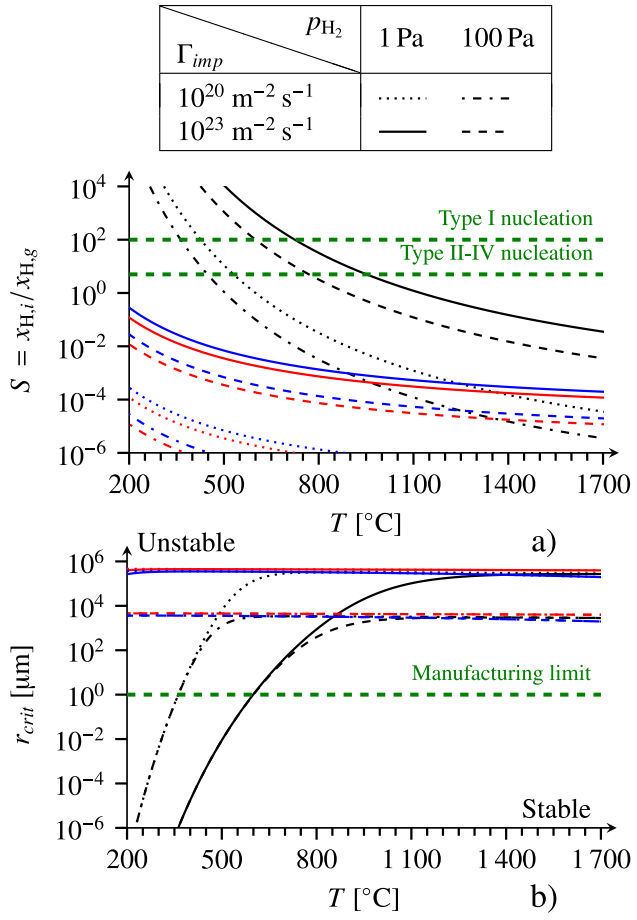

Fig. 6 **a** The hydrogen supersaturation ratio in LMs for Sn (black), Gallium (red) and Indium (blue) in steady state due to gas and ions, whilst neglecting radicals (**b**) and the critical bubble radius. Assumed is that $r_{imp} = 1$ nm for all LMs, according to SRIM there might a factor of 3 differences depending on T_i and the LM for $T_i < 10$ eV. Here 10^{20} m^{-2} s^{-1} and 10^{23} m^{-2} s^{-1} resembles nano-PSI and Magnum-PSI or a divertor respectively. It shows that Ga and In can suppress droplet ejection with a reasonable CPS ($r_{crit} > 1$ µm) independent of the temperature, whilst Sn would only be stable at higher temperatures

low hydrogen radical pressure $p_H < 1$ µPa. This is orders of magnitude lower than what would be expected in the divertor of a tokamak. Another option could be to increase the temperature to above 1100 °C. At this temperature, the evaporation of Sn becomes significant, leading to unacceptable core radiation. When considering ions only and neglecting the radicals in Fig. 6, there is a larger difference between the metals. Ga and In would essentially always be stable, even in a CPS with millimetre-sized pores. This is because the hydrogen solubility in these liquids is higher compared to Sn, see Fig. 2. This effect is not visible for the radicals due to the calculation of ΔG°_{H} and the associated reaction constant in Eq. (13). From this, it follows that LMs that have a higher hydrogen solubility will also dissolve more radicals with the same ratio, such that S is the same. Note that this is for steady state and that it will take longer to reach this equilibrium. There are three things that can be concluded based on the theory, which will be experimentally verified:

1. Droplet ejection is not unique to liquid Sn but can happen for all LMs, that do not strongly react chemically with hydrogen.
2. All LMs should eject droplets at the same pressure and temperature when exposed to hydrogen radicals only.
3. It should be possible to eliminate droplet ejection by increasing the temperature of the LM.

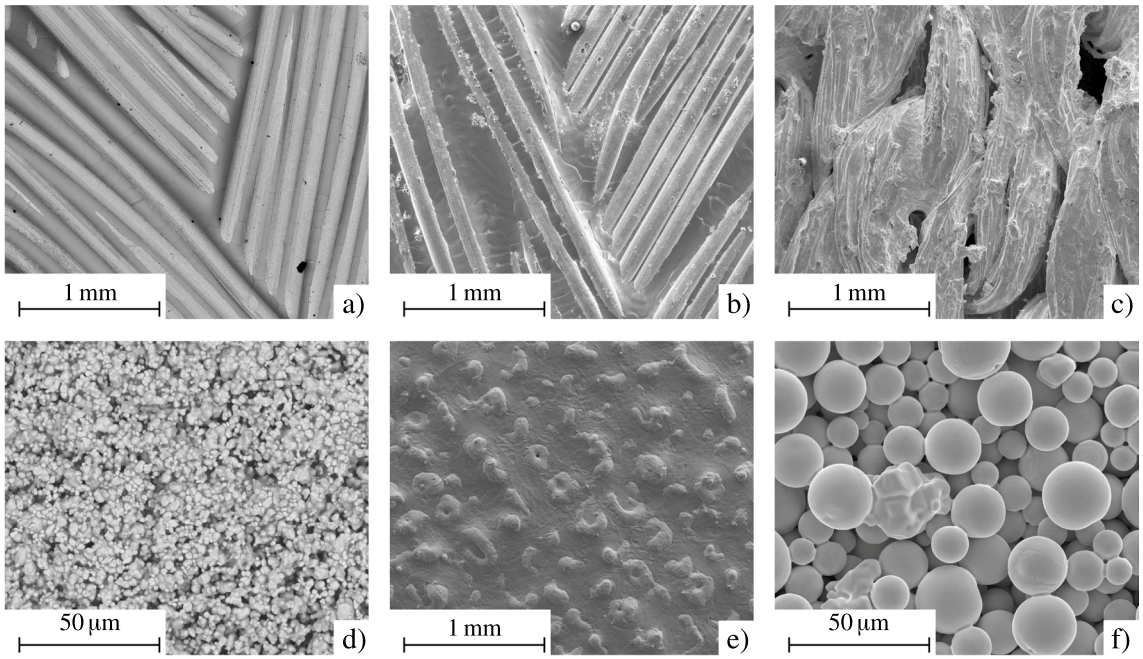

Fig. 7 SEM images with the wetted CPSs used. With **a** Braid 3B, **b** Braid 3C, **c** Felt, **d** sintered disc, **e** 3-D printed and **f** the sintered crucible. Tin be seen between the pores for both braids and the 3D-printed CPS. Whilst it is not visible in the sintered targets and the felt

In addition, different CPSs will be tested, which will have a different pore size, limiting the size that a gas bubble can have and therefore droplet ejection [6, 8].

Experimental Methodology

Targets

To measure the influence of the manufacturing technique, six different Sn-filled W CPSs were exposed to low flux plasmas using the cascaded arc plasma device nano-PSI, which is described in Sect. 3.2. The targets used are briefly discussed below and summarized in Table 3, whilst SEM images are shown in Fig. 7. The targets are deliberately underfilled, to prevent leakages by thermal expansion upon heating. The filling fraction gives the ratio between filled space and total available space and thus should be less than unity. The following CPS targets were used:

Table 3 General information about the CPSs used in this work

CPS	Pore size [µm]	Porosity	Mass Sn [g]	Filling fraction
Braid 3B	~ 150	0.61 ± 0.05	1.13	0.47 ± 0.04
Braid 3C	~ 150	0.62 ± 0.05	1.20	0.48 ± 0.04
Felt	~ 20	–	–	–
Sintered disc	0.65 ± 0.32	0.50–0.55	9	0.79 ± 0.04
3D-printed	100 ± 10	0.30	2.445	< 0.13
Crucible	< 25	0.35 ± 0.02	0.600	0.672 ± 0.001

For braids and felt the pore size is assumed to be equal to the wire diameter

1. W braids 3B and 3C, which are 8 × ∅150 µm wires, woven into braids by UKAEA. After this, they are outgassed and pressed together into a compact structure using hot isostatic pressing (HIP) by Proxima Powder Metallurgy, UK, similar to [65]. Sample 3B has a tighter weave than 3C, and thus the pore size of 3B should be smaller than 3C. They were wetted in a high-frequency vacuum oven ($T \approx 1000$ °C and $p = 10^{-5}$ mbar), 3B was filled with 1.13 g and 3C filled with 1.20 g of Sn. 3B is a rectangle with an area of 22.4 × 20.2 mm^2. 3C is a trapezoid with a height of 20.2 mm, a short side 21.8 mm and a 24.2 mm long side. Both braids have a thickness of 1.2 mm.
2. Woven W felts provided by ENEA, produced from ∅20 µm wires woven into a 110 µm diameter yarn. The resulting CPS felt is a compact and flexible material. After weaving, it was compressed using HIP to reduce the pore size, and subsequently cleaned with acetone. Wetting was achieved by placing the felts in an Sn pool in a vacuum oven at 1200 °C and 10^{-3} mPa for 1 h, which allows the capillary action to wick the target and ensure underfilling. For this test, a 36 × 26 mm^2 piece was cut, with a thickness of 4 mm. Cutting the felts to size after

wetting made it impossible to determine the mass of the Sn, porosity, and filling fraction.

3. A sintered W disc produced by Edgetech industries LLC, US, similar to those in [8, 66]. It has a thickness of 2.6 mm and ∅39.6 mm. The W powder used during the sintering process has a diameter ∅4.5−6 µm. The pore size was estimated to be 0.65 ± 0.32 µm [8]. Wetting was performed in a set-up at ASML Holding N.V., the Netherlands, similar to the 3D-printed target and sintered disc in [8]. A flux of 6×10^{21} at m^{-2} s^{-1} hydrogen radicals in a vacuum vessel at 16 Pa was used to remove tungsten oxides at a target temperature of > 700 °C, after which wetting is achieved at 400−500 °C. This allowed the disc to be filled with 9 g of Sn.
4. A W 3D-printed CPS produced by Dunlee (a brand of the Philips Company Group) using selective laser melting (SLM), similar to those described in [67]. It has a tree-shaped design which acts similar to the wick in an oil-lamp. On the bottom is a reservoir, which reduces in size towards the PFS. This allows the capillary force to always replenish the surface. On the surface, grooves are printed with a width of 100 ± 10 µm. Excess Li from previous experiments has been removed by placing the CPS in water overnight. Afterwards, it was placed in a vacuum oven at 1 mPa and 1000 °C for 2 h, to remove the tungsten oxides and residual water vapour. Wetting was performed similarly to the sintered disc, allowing it to be filled with 2.445 g of Sn. As a result of the SLM process, the tungsten itself has inherent porosities (porosity = 0.12 ± 0.01 [68]), in this case that allowed the tin to seep through the reservoir, and wet the rim at the outside of the CPS. Consequently, not all the Sn accumulated inside the reservoir and thus the filling fraction was lower than 0.13, the number given in Table 3.
5. A sintered crucible, where tungsten powder was sintered inside a crucible provided by Max-Planck-Institut für Plasmaphysik Garching. For the sintering, tungsten powder (grade "W-25/5 µm") from TEKNA Advanced Materials Inc, Canada was used. With this powder, 90 % has a diameter smaller than 25 µm. It was sintered for 1 h at 2027 °C. An open pore volume of 0.122 ± 0.001 mL was determined by estimating the amount of ultrapure acetone that could be accommodated before wetting the top surface. Filling of the CPS was performed using an ultra-high vacuum electron beam evaporator. The CPS was filled with 600 mg Sn, corresponding to a filling fraction of 0.67. More details about the manufacturing, wetting, and dimension can be found in [9], since a similar process was used.
6. A solid TZM (titanium zirconium molybdenum, > 99 wt% Mo) ∅30 mm reference disc, with a thickness of 2 mm. This was manufactured in-house and cleaned using ethanol.
7. Multiple TZM cups with an inner diameter of 27 mm. At the bottom, these have a ∅1.6 mm hole for a k-type thermocouple that is located 3 mm below the surface. This thermocouple was only used when the radical source was used. In the other cases, the thermocouple in the target holder arm was used. The cups were used to test various alkali metals (lithium, sodium and potassium) and post-transition metals (tin, indium, gallium, bismuth, and lead). New cups were used for each LM, which were filled with about 1.2 cm^3 of metal. Even if using the same process during wetting, the different metals will have a different contact angle and thus there will be a difference in the capillary action. Therefore, no CPS and no wetting was chosen as the most fair comparison. Furthermore, a cup wetted in the vacuum oven and filled with 5.5 g of Sn was used as reference to compare with the CPSs, which are expected to have less erosion than the cup. The exact values of the added LM mass is given in Table 6.

All targets were mounted using a stainless steel clamping ring with a ∅22 mm hole. Because of this, the plasma-facing area is the same in all targets, except for the crucible, even though their dimensions vary. The clamping rings were reused during these experiments; therefore, they were cleaned using diluted CitraNOX®with a Scotch-Brite®pad and abrasively blasted. The CPSs were surrounded by four ∅12 mm

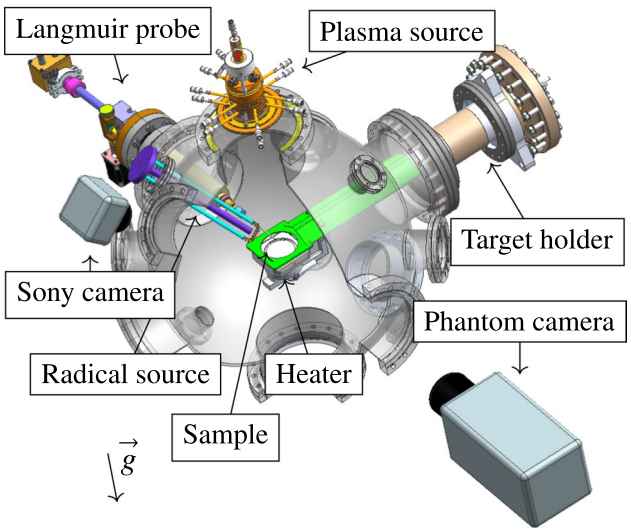

Fig. 8 A schematic overview of nano-PSI, showing all relevant components and diagnostics. Only three-quarters of the vacuum vessel is shown, to improve the visibility of the other components. This device was either used to generate a plasma or radical flux. When a plasma is generated the radical source was removed and the Langmuir probe was not used during liquid metal exposure, both were replaced with a blind flange. During the shadowgraph measurement, the Langmuir porthole was replaced with a laser, as shown in Fig. 9

stainless steel witness plates (WPs), placed 25 mm from the centre of the target to the centre of the WP.

The measurement and comparison of droplet ejection is not straightforward; several aspects must be considered. There may be various sizes of droplets, and they may land close to the target or further away. Therefore, the total erosion from the targets is measured using a scale and the deposition of LM on the nearby WPs using Rutherford backscattering spectroscopy (RBS). To still be able to compare the erosion of the crucible with the other CPSs, the results are normalized over the area of the PFS (A_{PFS}) and exposure time.

Nano-PSI

Plasma exposures were performed in nano-PSI at DIFFER. The set-up of this device is shown in Fig. 8. It consists of a vacuum vessel with an outer diameter of 450 mm. A plasma can be generated using a cascaded arc source attached to the top of the vessel. A constant gas flow of 3 SLM through the source was controlled using an MKS MF1 mass flow controller. The discharge current was 50 A and the typical cathode voltage was 155 V. To start the plasma, first an Argon (Ar) plasma has to be generated, after which the gas through the source is slowly ($\approx 1-2$ min) changed to pure hydrogen. Whilst there is an Ar plasma and during the transition, the targets were shielded with a TZM shutter, not shown in Fig. 8. The targets were not biased, to minimize mass loss from sputtering. The targets were heated using the Model 102916 2" Sample Stage and the 102915 2" 1200 °C O2 Heater Dock Assembly from HeatWave Labs Inc, USA [69].

Diagnostics

The pressure in the vessel during exposure was measured using an MKS Baratron 627F gauge to be around 60 Pa. The electron temperature and density were determined using a double Langmuir probe. This consists of 2 tungsten wires with $\varnothing = 0.5$ mm and a length of 5.9 mm. T_e and n_e were measured when the no target was mounted inside nano-PSI, at the position where the PFS was located once a target was placed inside the vacuum vessel. During this study $T_e = 0.26 \pm 0.1$ e V and $n_e = 8.0 \times 10^{16} \pm 0.5 \times 10^{16}$ m^{-3}. With the electron temperature and density known, the ion flux can be determined using Eq. (22). In this case, $\gamma = 8/6$ and the mass of the ion $m_i \approx 3m_u$ where m_u is one atomic mass unit, since H_3^+ is considered the dominant ion species when using a cascaded arc source [48]. From this, it follows that $\Gamma_i = 2.2 \times 10^{20} \pm 0.2 \times 10^{20}$m^{-2} s^{-1}. There were two cameras used, a conventional camera, Sony IMX586, with a spatial resolution of 100 µm and recording frequency of 60 Hz. The other was a high-frequency Phantom camera (Vision Research Phantom v12.1 camera). This has a recording frequency of 5 kHz and spatial resolution of 20 µm.

Radical Source

The radical source in Fig. 8 was built in-house. It works by flowing hydrogen gas over a hot tungsten wire. The mass flow was controlled by a mass flow controller (EL-FLOW Select F-201CV from Bronkhorst High-Tech B.V., The Netherlands), which can ensure constant gas flow between 7−1000 sccm with intervals of 1 sccm. The ∅0.5 mm W wire was coiled with a winding diameter of 5.5 mm and a total wire length of about 140 mm. The radical flux was estimated using:

$$\Gamma_H = f_{dis} f_{hit} \Gamma_{H_2} = \frac{10^3}{60} f_{dis} f_{hit} \frac{N_A \rho^{\circ}_{H_2} \dot{V}[sccm]}{A_{PFS}} \tag{31}$$

with Γ_{H_2} the H_2 flux, $\rho^{\circ}_{H_2} = 0.08988$ kg m^{-3} [47] the density of H_2 gas a standard conditions and $\dot{V}[sccm]$ the volumetric gas flow. The later was determined using a mass flow controller in [sccm], all other variables are in standard SI units. Hydrogen molecules hitting the wire are assigned a probability, f_{hit}, based on geometry, a value of 0.25 was used. The dissociation fraction, f_{dis}, represents the likelihood that a hydrogen molecule dissociates upon contact with the tungsten wire. This dissociation probability is temperature-dependent [70], which was measured by comparing the electrical resistance to values found in the literature [71]. Voltage differences were measured using the 4-Point Probe method, to only determine the resistance of the hot tungsten wire. Using this approach, it was determined that the wire was ≈ 1900 °C whilst applying a power of 120 W. At this temperature $f_{dis} = 0.06$, furthermore, this does not significantly change with the pressure and thus the flow speed [70].

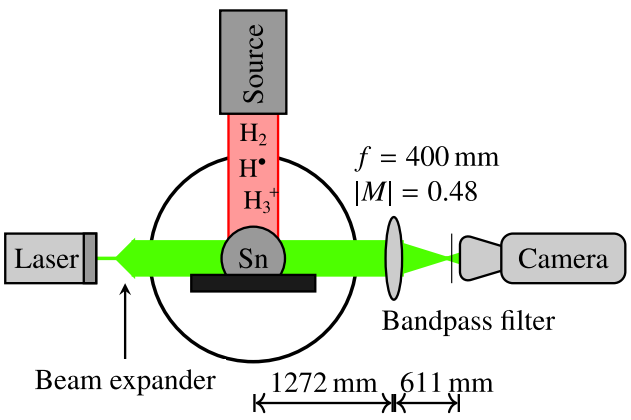

Fig. 9 A schematic overview of the shadowgraph set-up in nano-PSI. With this set-up, an image of the shadow of a bubble collapse can be made with high spatial and temporal resolution

Shadowgraph

Shadowgraph was used in this work to get sharp high-frequency images of the ejection of an Sn droplet and to compare it to the shape expected when a gas bubble collapses. Usually, this technique is used to observe inhomogeneous flow in a transparent medium. However, in this case, it was used to enhance the contrast of the ejected Sn droplets. A schematic cross-section of the set-up is shown in Fig. 9, where the laser used the same optical port as the Langmuir probe in Fig. 8. To get a homogenous light source, the light bundle from a 4.5 mW laser (Thorlabs CPS532) with a wavelength of 532 nm was expanded 20 times by a beam expander (Melles Griot). This light travelled through the vacuum vessel of nano-PSI, where part of it was blocked by a drop of liquid Sn resting on a flat tungsten tile. The remaining light was focussed, using a lens with a focal length of 400 mm. The shadow of the droplet is projected with magnification $|M| = 0.48$ to the Phantom camera, resulting in a resolution of 24px mm^{-1}. Between the lens and the camera was a band-pass filter, with a central wavelength at 532 nm, to block all light that does not originate from the laser, such as the light emitted by the plasma.

Glovebox

Sample handling of alkali metals was done using a PureLab High Efficiency glovebox from Innovative Technology, Inc, USA. This was filled with argon. The oxygen and water concentration was monitored and remained below 1ppm.

Post-mortem Analyses

Rutherford Backscattering Spectrometry

Rutherford Backscattering Spectrometry (RBS) is a technique that uses a high-energy ion beam to determine the composition and areal number density, i.e. atoms per area ($n' = N/A$), up to a few micro meters probing depth. Part of the ions fired at a WP will scatter and can be detected. The energy of the scattered ions are determined by the material on which it scatters. In this work, RBS was used to determine post-mortem how much metal was deposited on the WPs during plasma exposure. For this purpose, the stand-alone ion beam analysis station (IBAS) in DIFFER was used. This facility is connected to a 3 Me V singletron ion accelerator by High Voltage Engineering Europa B.V., the Netherlands [72]. In this work, H^+ ions were accelerated to 2.1 Me V with a spot size of 1×1 mm^2, allowing a detection depth of Sn up to 16 µm by a surface barrier detector. In the IBAS the incident angle of the beam on the WP $\alpha = 0°$, exit angle $\beta = 10°$ and scattering angle $\theta = 170°$. To calibrate the energy of the detected ions, pure silicon, chromium, silver, and zinc reference samples were used, together with a silicon sample coated with 662×10^{15} at cm^{-2} platinum. The data is analysed using the ion beam analyses (IBA) software Datafurnace (NDF) [73]. This software can optimize the layer thickness and composition to match the experimental results. The layers are given a composition between the substrate and the deposited metal to account for the fact that droplets are not distributed homogeneously. Here, a maximum of 3 layers on top of an iron (Fe) substrate was used. The layers in NDF were not thinner then the resolution limit calculated by ResolNRA [74]. Nano-PSI has been contaminated by Sn, therefore, even when a target was not filled with tin, Sn was included in the layers. As a result the layers consisted only of Fe, Sn, and the LM tested. An example of why it was important can be seen in Fig. 17. A disadvantage of the use of RBS is that atoms with atomic number close to each other are difficult to distinguish, in this work it was not possible to differentiate between In ($Z = 49$) and Sn ($Z = 50$). Since there was always Sn presence in nano-PSI the RBS results from the In case might be overestimated.

Mass Balance

The mass of the targets was measured before and after exposure using a high precision mass balance (NewClassic MF, model MS105DU from Mettler-Toledo B.V., the Netherlands). This is calibrated every year and has a measurement error of 0.01 mg up to 42 g, above that an error of 0.1 mg is used.

Results and Discussion

Shadowgraph

Figure 10 shows four frames of the fast-imaging video made using the shadowgraph set-up in nano-PSI. For this representation, the background noise has been removed using the cross-platform image editor GIMP 2.10.32 by increasing the contrast first after applying a brightness threshold. The first image shows a drop of liquid Sn partially wetted on a W substrate, just before the gas bubble inside the drop collapses. The second image shows a crater in the liquid just after the collapse of the bubble. This collapse is usually associated with the formation of thin film droplets. These were not captured on this video and if they were present they are either too small (< 42 µm) or fast (> 80 ms^{-1}) to capture. Another possible explanation is that film droplets did not form, as has been observed with other liquids [57]. Afterwards, the surface restored in the third image, where the formation of a Worthington jet can be observed. Four sub-millimetre sized

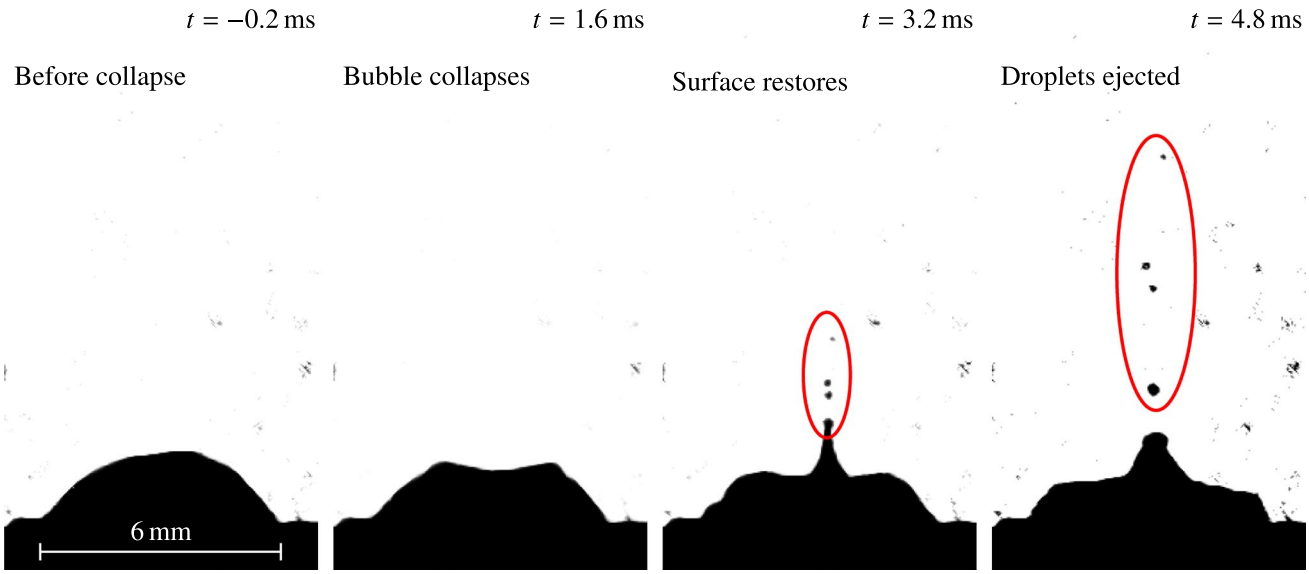

Fig. 10 The collapse of a gas bubble, as shown by the shadowgraph set-up in nano-PSI. The time $t = 0$ s is set at the collapse of the bubble. These pictures show a classical image of droplet ejection by the collapse of a gas bubble

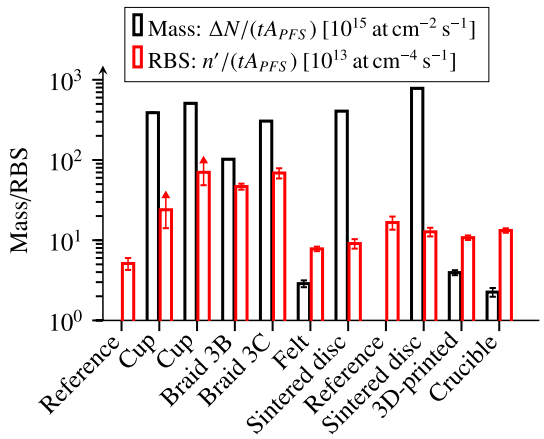

Fig. 11 The area averaged erosion rate of the targets exposed to nano-PSI for 30 min at 500 ± 30 °C as determined from the Sn on the WPs by RBS and the Mass balance. The targets are placed in the same order as they were exposed to nano-PSI. The error bar for the RBS is mainly influenced by the statistical error on the four witness plates. Due to Sn contamination in the vessel also a significant amount of Sn could be observed for the references. The arrow on the error bars for the RBS on the cups indicates that this is a minimal value

droplets were ejected from the surface once the jet fell apart. These droplets are highlighted by the red ellipse in the third and fourth images. The droplet at the top has a speed of approximately 4 ms^{-1} between the last two pictures. To summarize, these shadowgrams managed to capture a classical gas bubble collapse with an LM as described in Sect. 2.6 and therefore provide visible evidence that droplet ejection is caused by the collapse of gas bubbles.

Comparison of Different CPS Designs Under Plasma Exposure

The different CPSs were exposed for 30 min at 500 °C to a hydrogen plasma in nano-PSI. Due to the plasma exposure, the liquids were heated, which could be partially compensated by reducing the power of the heater. This still resulted in a temperature difference of ±30 °C between the different metals, as measured by the thermocouple in the target holder. The temperature of 500 °C and the low ion energies ensure that no mass loss via sputtering or evaporation should be expected, thus only mass loss by droplet production should be observed.

Reference and Cups

Before exposing the CPSs, first the reference W target without Sn and second a cup filled with Sn were exposed. The resulting area-averaged erosion rate for both is given in Fig. 11. Already, $n' = (92 \pm 16) \times 10^{15}$ at cm^{-2} ($n'/(tA_{PFS}) = (5.13 \pm 0.17) \times 10^{13}$ at cm^{-4} s^{-1}) of Sn was measured on the WP around the reference target. This is because nano-PSI was already contaminated with Sn by previous experiments. This also means that the order of exposure of the CPSs is important to keep in mind, since they increase the Sn contamination in nano-PSI. The Sn layer on the WPs increased by a factor of three between the repeatability tests with the cup, whilst the mass loss increased by 30%. A possible explanation why there is more erosion in the second experiment could be because the same cup was used, and thus the liquid might have been saturated with hydrogen

during the second test. Furthermore, initial plasma exposure may have removed oxides; this will be discussed in more detail in section "Round 2" . Furthermore, the WPs surrounding the cups had big Sn drops visible by eye (> 1 mm). For a Sn layer thicker than 16 µm, the Sn peak overlaps with the Fe substrate and thus it becomes impossible to determine the correct value. Arrows are added in the error bar of Fig. 11, to indicate that the given value should be viewed as a lower bound. During the first exposure, the limit was reached on only 1 WP, whilst this limit was reached twice during the second exposure.

Braids

A significant amount of Sn has been measured on the WPs of the braids, which also had clear Sn droplets visible by eye, yet smaller than for the cup (< 0.2 mm). The mass loss from braids 3B and 3C was approximately 5 and 1.5 times lower, respectively, compared to the previous cup. Both the RBS and the mass loss indicate that braid 3B outperformed 3C. This makes sense since in 3B the weaves were pressed tighter together, which would result in a smaller pore size.

Felt

The felt had the lowest mass loss of all CPSs, with only 1.02 mg. Moreover, the least amount of Sn has been observed on the WPs around the felt. However, the felts went from a shiny metallic colour towards black. This could indicate that during exposure, the Sn at the PFS was exhausted. Furthermore, there were still droplets visible both on the clamping ring and the WPs. This indicates that even in this case there was droplet ejection.

Sintered Disc

After the felt, the sintered disc was exposed. The disc performed similarly to the felt when looking at the RBS results, but had one of the highest mass losses. Six frames from the video looking at this target are shown in Fig. 12. It shows Sn "sweating" from the CPS and forming two pools on the surface. One of these preferred wetting the clamping ring rather than the CPS. The other pool did not wet the clamping ring, but was reabsorbed by the CPS 21 min after its formation. This pool was the main source of droplet ejection, according to the video. This indicates that indeed a CPS can play a suppressive role if the liquid is properly confined within its pores. Additionally, drops emerged at the bottom of the disc, following the plasma exposure, Sn drops were observed at the holder below the CPS. Therefore, almost all mass loss from the sintered disc measured with the scale can be attributed to "sweating". This emerging of Sn from the CPS was also observed in GLADIS and OLMAT [66, 68] and was attributed to the thermal expansion upon heating.

As a result a second exposure was made, as in this case all the excess Sn should have been lost such that only droplet ejection from the pores takes place. Nano-PSI was used for the re-wetting, in this case, the clamping ring was completely removed to ensure that the complete PFS was exposed. To start the plasma, we started with argon before switching to hydrogen. The evolution of this can be seen in Fig. 13. Initially, Sn droplets were observed to sweat from the disc whilst exposed to an argon plasma. As soon as H

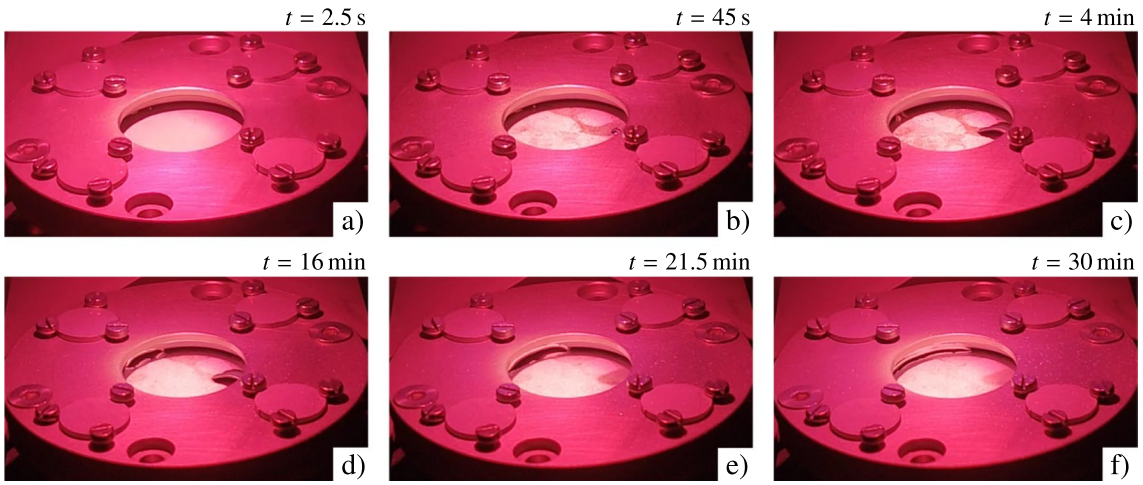

Fig. 12 Time-lapse from the Sony camera of the plasma exposure of the sintered disc. The surface appeared clean and shiny at the start of the discharge. Within a minute, a pool of Sn started to form on the PFS, together with brighter and darker spots. Droplet ejection is only observed by the camera from this pool. After 4 min, a second Sn drop wetted the clamping ring. The first pool continued to grow and reached its maximum extent after 16 min, subsequently it gradually reduced again. 5.5 min later, the pool is completely absorbed again by the disc. In the meanwhile, the drop wetting the ring continued to grow until the end of the discharge

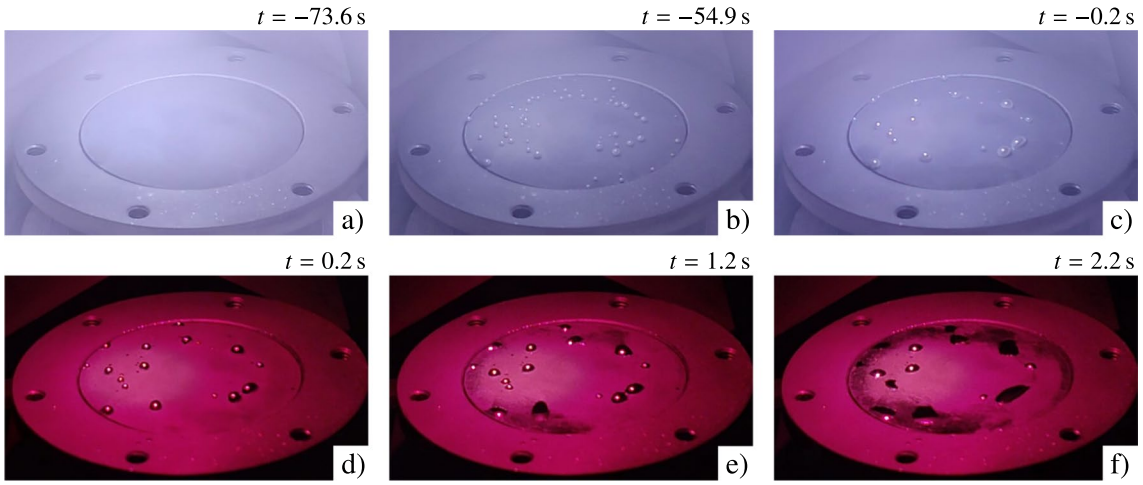

Fig. 13 Time-lapse from the Sony camera during the wetting of the sintered disc in nano-PSI, at $t = 0$ s the plasma switched from Ar to H. Whilst exposing to Ar, Sn droplets started to appear on the surface of the disc in multiple places. These drops formed almost perfect spheres and thus were not wetting the CPS. Over time, some of these drops merged. As soon as H is added to the plasma, the drops wetted the surface, forming pools of liquid. From these pools, droplet ejection was observed within 2.5 s from switching

was added, the surface wetted and within 2.5 s, and droplet ejection started from the wetted Sn surfaces. Hydrogen is known to remove tungsten oxides and therefore enhance wetting [75]. The centre of the disc appeared relatively free of Sn pools, which accumulated on the edge of the disc.

Since this was not as effective as intended, the disc was successfully re-wetted in the vacuum oven. Before redoing the exposure, the vacuum vessel of nano-PSI was cleaned using diluted CitraNOX®and Scotch-Brite®pad. Therefore, a new reference test was performed. In Fig. 11 it can be seen that the amount of Sn measured on the WPs was about 3 times more than in the previous case. This could be due to the other exposure and insufficient cleaning. During the second exposure of the disc, no pooling was observed on the PFS. This time, Sn droplets only formed at the bottom of the CPS, wetting the target holder. Furthermore, the sintered disc was damaged and a 22 mm (direct line between both ends) crack formed. The most likely reason for this is due to thermal cycling. This disc is known to be fragile, and similar discs were damaged during other experiments in OLMAT [66]. This increases the effective pore size and thus could result in additional droplet ejection.

3D-Printed

The 3D-printed CPS performed the best after the felts, however, about 40% more erosion was measured using the RBS and the scale. Furthermore, some Sn droplets were observed on the clamping ring and WPs similar to the Felts. The filling fraction in this target was the least of all tested CPSs. Furthermore, the pore size increased away from the PFS. This might have resulted in degassing internally, leading to fewer droplets ejection.

Crucible

The last CPS tested was the crucible, which also started to sweat similarly to the disc, even upon heating. Therefore, it was decided to remove the sweated Sn, with a total mass of 20.05 mg before exposure to hydrogen plasma. During a second attempt, Sn sweating was observed again and 12.38 mg could be removed. Due to thermal expansion between 20−500 °C, a maximum of 41.5 mg (6.9%) could theoretically escape the CPS [76]. It is remarkable that not all Sn escaped the CPS during the first heating cycle. In the SEM image, see Fig. 7, it can be seen that the PFS is not wetted with Sn in the sintered targets unlike the other CPSs, except for the Felt. A possible explanation is that thermally expanding Sn comes into contact with tungsten oxides on the PFS, on which it cannot wet. Whilst cooling down and thus contracting, the remainder of the Sn returns to its original position. Some pores which were initially wetted may have dried out and oxidized, whilst sweated droplets were removed. It was therefore decided to reheat the crucible again, but this time in the glovebox. However, even in this environment, Sn sweated from the crucible and a total of 45 mg was lost during three heating cycles. By now, already 13% or 78.17 mg of Sn was lost due to sweating. Given that a similar manufacturing technique was used for the disc and to avoid cracking the sample due to thermal cycling before exposure, the process was stopped at this point. Whilst heating in nano-PSI prior to the exposure, spherical Sn balls formed on the CPS again. During exposure, more emerged,

which wetted the rim of the crucible and from which droplets were ejected, similar to the disc and previous experiments with the crucible [9]. In that case, a meniscus of liquid Sn was formed at the contact line between CPS and crucible, and was also suspected to be a potential source of droplets. However, this time it did not wet the clamping ring, and thus the weight loss measurements are accurate. The total mass loss was the least for the crucible with only 0.8 mg and the total Sn amount was most similar to the disc. However, the total plasma-facing area was also four times less than the others. Therefore, the area-averaged erosion was three times higher compared to the felts.

Summary of Different CPS Designs

Overall, it can be concluded that droplet ejection has occurred on all CPSs. Furthermore, in can be largely influenced by the formation of a free surface layer on top of the CPS. It is likely that in a fusion reactor, over time, these pools would disappear, just as for the sintered disc in Fig. 12. From the theory described in Sect. 2 it was predicted that a larger pore size should lead to more Sn erosion. In Fig. 14 the data from Fig. 11 is shown with the pore size on the x-axis. There appears to be an increase in mass loss and Sn on the WPs with the pore size, although the exact fitting parameters are not reliable.

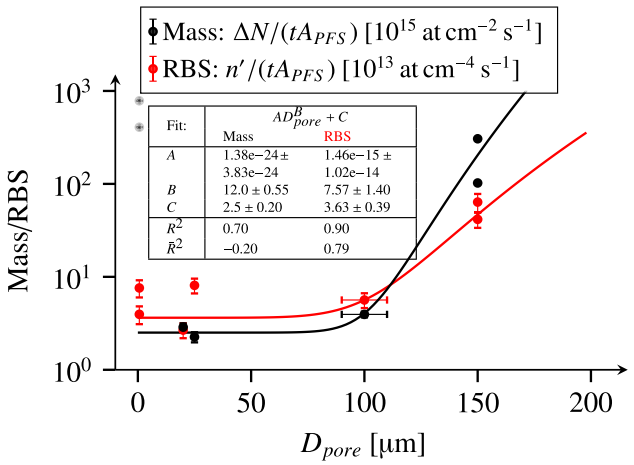

Fig. 14 Comparison of the area averaged erosion rate for the various CPS targets from Fig. 11, reordered by pore size. The table shows the fitting parameters and variance of a power law with offset, with the pore size, or pore diameter D_{pore} [μm]. Figure 3 can be used to relate the pore size to the different CPS targets. It also shows the coefficient and adjusted coefficient of determination (R^2) and ($\bar{R}^2$) respectively. For the mass loss the sintered disc is omitted from the data set, since most of the mass was lost to wetting the clamping ring, these points are made transparent. As a result, not enough data points are present for a reliable fit. For the RBS analysis, the first reference result has been subtracted as background. In both cases there appears to be a positive trend with the pore size, although this is highly influenced by the data points from the braids

Comparison of Different Liquid Metals Under Plasma Exposure

Round 1

The previous section already showed that the amount of Sn deposition on the WPs during a 30 min discharge was already too much to quantify by the RBS. Furthermore, evaporation starts to become significant for some metals. For Bi and Pb it is ∼ 1 mPa and for Li ∼ 0.5 Pa at 500 °C. Therefore, the exposure time was reduced to 10 min and an initial temperature to 300 °C for the comparison between the LMs. It took about 5 min before Pb melted at 327.5 °C, all other metals were liquid from the start. During exposure, the temperature was observed to slowly increase due to the heat flux of the plasma to 370 ± 10 °C, even with the heater completely off. Initially, the cups were not wetted, as it could not be guaranteed that the contact angle between the

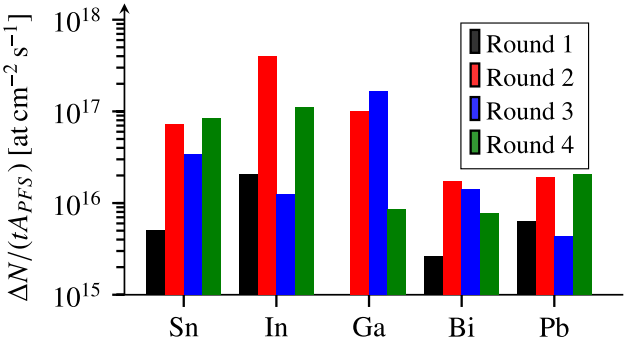

Fig. 15 The area averaged erosion rate as determined by the mass loss for 5 post-transition metals after exposure to nano-PSI at T = 300 °C–370 °C ± 10 °C

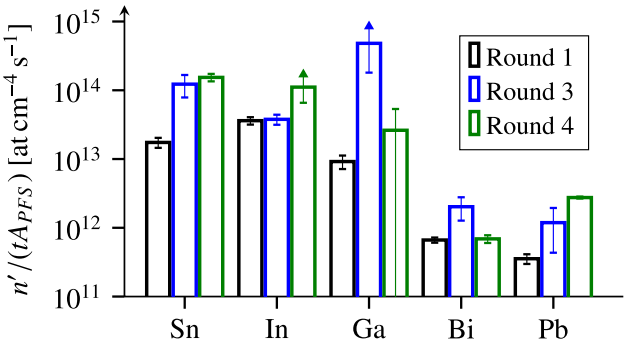

Fig. 16 The area averaged deposition of Sn on the WPs as measured most-mortem by RBS for 5 post-transition metals after exposure to nano-PSI at T = 300 °C–370 °C ± 10 °C. Indium peak are difficult to distinguish from Sn peaks using RBS. Furthermore, the In peak after the new cup and Ga after wetting are at least that high, this is indicated by making the error bar an upwards pointing arrow

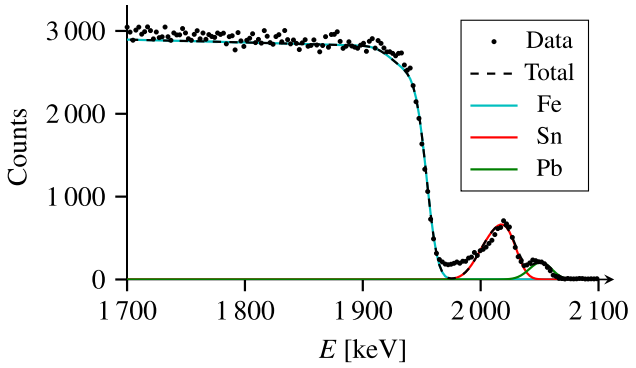

Fig. 17 Example of the results of RBS on one of the WP surrounding Pb after round 3. The experimental data is indicated by the black diamond marks, and the total simulated value by the black dashed lines, which can be subdivided in the individual contribution from each element. Even though this was an experiment with a Pb cup, the Sn peak is bigger, resulting in a $140 \pm 7 \times 10^{15}$ at cm^{-2} and $7.0 \pm 0.410 \times 10^{15}$ at cm^{-2} for Sn and Pb respectively

liquid and the cup would be the same in all cases. During those tests, some droplet ejection was observed for all liquid metals except Bi. For Bi rather than droplets being ejected, the liquid would be displaced when a gas bubble collapses. During this event, there might have been droplet ejection, but this was not confirmed with the conventional camera. Additionally, because of this movement, the plasma could also partially see the cup, rather than the liquid metal, and thus the plasma-facing area was not always the same. This is also confirmed in Figs. 15 and 16, where the area-averaged mass loss rate and deposition on the WPs are shown. These are an order of magnitude lower than for the Sn cup in Fig. 11. It should be noted that, due to the small difference in atomic number, In is indistinguishable from Sn when using the RBS, and thus the number shown in Fig. 16 might be higher than the real amount of In on the WPs. To highlight this, an example of a WP with Pb is shown in Fig. 17, where the amount of Sn was 20 times more than for Pb.

Round 2

Due to the observed movement of the liquid, the LMs needed to be wetted to the cup, for a better comparison between the liquids. This was done in nano-PSI, similar to the other test. No clamping ring was used during wetting, to allow the plasma to wet the entire cup. As a result, the PFS increased from ∅22 mm to ∅27 mm. During this exposure it took Sn 13 min, In 9 min, Ga 10 min, Bi 10 min and Pb 18 min to wet their respective cups. The mass loss during this exposure was added in Fig. 15. The case of In is illustrative in understanding and interpreting the observations here, and 8 frames of camera video are shown in Fig. 18. At the start of the discharge, the metal had a dull grey colour on the surface. After about 3 min, a shiny hole appeared in the centre of the In surface. This region grew until a droplet was ejected, which was observed to come from that region. It takes another 75 s before the next droplet is ejected from the same location. After this, it continued to eject droplets, whilst the ejection frequency increased. It is notable that no droplets were ejected from the dull regions. They always originated from the shiny part, or the interface between the two. The most likely explanation for this is that the metals are oxidized before exposure, which is slowly removed by the hydrogen plasma. These oxides form a solid barrier for the hydrogen to penetrate towards the liquid metal. Gas bubbles could form in solid metals, but do not cause droplet ejection [24]. Only after a hole in the oxide layer had formed, could hydrogen dissolve in the liquid and gas bubbles nucleate. Similarly, bubbles cannot penetrate the oxide layer and so can only be released from the shiny oxide-free region. Something similar happened to all other metals.

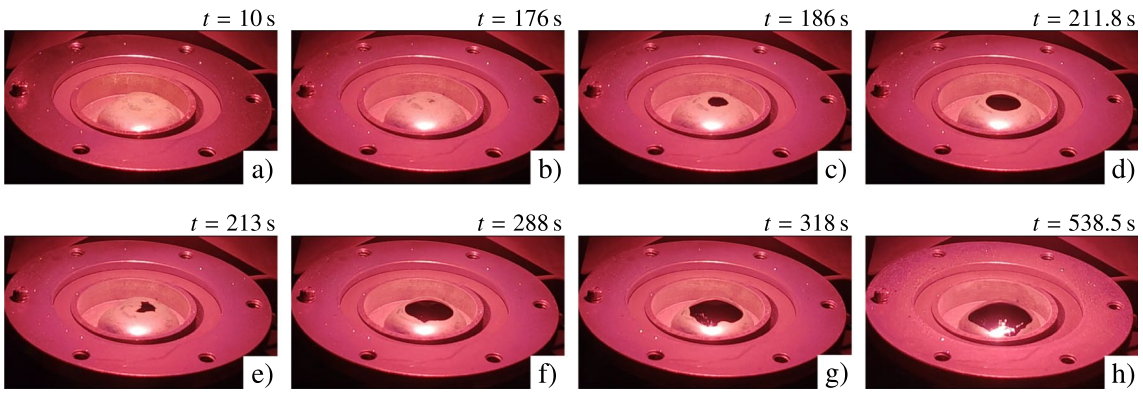

Fig. 18 Example of the influence of an oxide layer on the delay of droplet ejection for In. It takes 176 s until a hole in the oxide layer forms, which starts to grow until a first bubble bursts directly after 211.8 s. After 213 s, the surface stabilizes and the hole continues to grow. After 288 s droplets start to be ejected, which increases in frequency

Round 3

After exposure to nano-PSI, the liquid in the cups was thoroughly stirred for 5 min at ≈ 300 °C in the glovebox to degas the dissolved hydrogen. For round 3, the exposure time was increased to 20 min, to ensure that oxide layers would be removed if they appeared again. The results of these cases are shown in blue in Figs. 15 and 16. However, what happened was similar to round 2, on all metals there was an oxide layer. For both Sn and Ga, a hole would form and droplet ejection was observed similar to Fig. 18. For the others, the oxides were not removed, even after 20 min of exposure. In the case of In, there was one big drop that did not land on the WPs, but instead on the clamping ring.

Round 4

Since there was still an oxide layer, new cups were used for round 4 and wetted in the vacuum oven. The high temperature in the oven $T > 1000$ °C should remove oxides and ensure that the cup is wetted. However, all but Sn still had an oxide layer, which could form during transport between the oven and nano-PSI. This layer was removed by sputtering Ar in nano-PSI while the target was biased to −20 V. They were not heated and, thus, were solid once the exposure started. It took 6.5 min to clean In, 10 min for Ga, 8 min for Bi, and 13 min for Pb to be clean. Subsequently, they were exposed for 20 min of deuterium, starting at 350 °C. During exposure, the temperature increased to a maximum of 400 ± 10 °C, minimizing the temperature difference whilst exposed. Afterwards, the same cup was exposed to an argon plasma for the same amount of time, and no significant mass loss was measured. LM was also not deposited on the WPs, not even Sn, whilst this was always present even when another metal than Sn was exposed. Whilst switching from argon to deuterium, a small oxide layer was still formed on the liquid metals. However, this could be removed much faster this time for all metals, except Ga. All others showed a clean surface from which droplet ejection was observed. In the case of Ga, there remained a layer on which still some droplet ejection was observed on the camera.

Overall Impression Post-transition Metals

In summary, the different properties and behaviour of the liquid metals make quantitative comparison between them difficult. What at least can be concluded is that all tested post-transition metals can eject droplets, but that there may be an incubation time based on the wetting of the liquid to the cup and the presence of an oxide layer. This also holds for Sn, and thus may influence the comparison between the different CPSs in the previous section. This might also explain why in some papers droplet ejection was not observed, for example in FTU [25], where the exposure time was only 1.6 s, of which 1.3 s corresponded to the flat-top phase. During this time, the maximum surface temperature reached > 1600 °C, which also increases the hydrogen solubility as discussed in Sect. 2. Furthermore, Bi and Pb are seemingly more resistant to droplet ejection. Both have a high mass density that might prevent the droplets from being ejected further away. Hence, they can land back into the cup rather than on the WPs, and they are not measured on the RBS or with the weight loss.

Alkali Metals

Additionally, three alkali metals were exposed to nano-PSI: lithium, sodium (Na) and potassium (K). Li was exposed for 20 min with a starting temperature of 300 °C, just like the post-transition metals. During this exposure, 5 mg or 9×10^{16} at cm^{-2} of lithium was lost. The plasma emitted a red light during this discharge, indicating the presence of the Li I line at 670.78 nm. Although the surface became shinier, no droplet ejection and no movement of the liquid was observed. Furthermore, the liquid appeared to be well wetted to the cup. The starting temperature for Na was lower with 100 °C, within 4 min a yellow glow appeared above the cup, indicating the presence of Na I lines at 589.0 nm and 589.6 nm. Therefore, it was concluded that Na was strongly evaporating in the plasma. After a total exposure time of 6.5 min the discharge was ended. During this exposure, no droplet ejection was observed, and a mass gain was measured. Similar observations were made for K, which was exposed at a starting temperature of 150 °C, where a yellow glow formed again, and the discharge was ended after 5 min. During this time 119.5 mg or 1.6×10^{18} at cm^{-2} was lost. To measure the mass loss, the cup with the liquid has to come into contact with the ambient air whilst transporting. During this time, the alkali metals can react with water and oxygen. This can explain the mass gain for Na, and means that the mass loss during exposure is probably higher than the quoted numbers above.

Radical Source Exposure of Tin and Gallium

Cups filled with Sn and Ga were exposed to the radical source in nano-PSI, in order to compare with the three predictions outlined in Sect. 2.7. The gas flow through the source was initially set to 10 sccm and the cups were heated to 400 °C. This is the temperature the cup would reach without the heater on, just from the heat of hot tungsten wire. In the case of Sn, droplet ejection started within 2 min. The heater was turned on and the droplet ejection stopped once the temperature exceeded 630 ± 30 °C. When the heater was turned off, droplet ejection would start again once the temperature reached below this point. This heating and cooling was repeated three times to clearly see which temperature

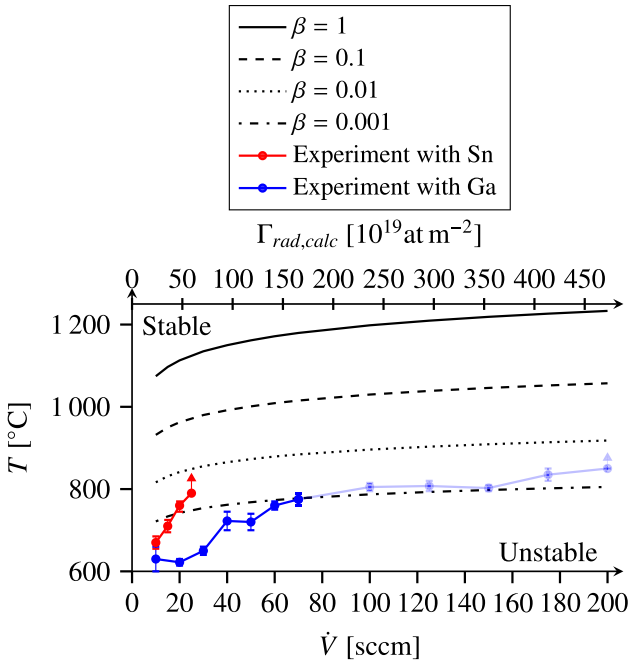

Fig. 19 Stability curves for both Ga and Sn as measured using the radical source in nano-PSI. Droplet ejection is only possible below the curves, whilst no droplet ejection is observed above them. After some time, gallium flowed out of the cup, due to the enhanced wetting. The upwards pointing error bars indicate that droplet ejection was not prevented and that the stability curve is above this line. These data points are indicated in transparent blue. In black the prediction is shown for a given correction factor β where type II–IV nucleation is assumed to be sufficient ($S = 5$) in Eq. (25). Γ_{rad} was predicted using Eq. (31), but this value may be overestimating the true radical flux

was the tipping point. At 25 sccm and above for Sn, the temperature could not increase to a point where ejection could be prevented, for Ga this point was at 200 sccm. These points are added with an arrow in Fig. 19 to indicate that the droplets are still ejecting. It should be mentioned that in the case of Ga, the LM started to slowly leak out of the cup by wetting over the edge of the cup. These points are indicated by the transparent colour in Fig. 19. In this graph, four additional curves are added where $S = 5$ and β is varied in Eq. (25) and the predicted radical flux from Eq. (31). This would be the transition temperature between droplets and not droplets. This would indicate that Henry's law (11) could overestimate the steady-state hydrogen molecular fraction due to the radicals by three orders of magnitude. This number has to be taken with care since the radical flux was not directly measured and in reality it might be lower. This could be because some atoms recombine before hitting the LM, or not all atoms are hitting the cup. Even with $\beta = 0.001$, there will droplet ejection in a diverted plasma due to the radicals. In Fig. 5 the graphs for $\beta = 1$ and 1 Pa can also be interpreted as $\beta = 0.001$ and 1 mPa. Even though the exact transition temperature could not be predicted, this graph can already confirm two important hypotheses which were predicted by the theory. Firstly, hydrogen radials are sufficient to get droplet ejection and secondly that this can be prevented by increasing the temperature.

What Do These Results Mean for a Liquid Metal Divertor?

According to the theory described in Sect. 2, there are a couple of things that can be done to mitigate bubble formation in relation to operation of a Sn-based liquid metal divertor in a future fusion reactor:

1. *Increase the gas pressure:* In sodas and champagne no bubbles are present whilst the bottle is closed, this is because the solubility limit is not reached at these pressures [51–53]. In the case of hydrogen and liquid metals, Sievert's law (Eq. (27)) can be used to determine the additional hydrogen that can be dissolved, explaining the inverse square root scaling with p_{H_2} in Eq. (25). For a nuclear fusion reactor, there are options for gas puffing to increase the pressure, leading to detachment of the plasma. But this is limited, as puffing too much gas could cool the plasma. From Figs. 5 6 it can be deduced that the required pressure needs to be above 1 bar, while even in the best-case EU-DEMO scenario the pressure would be 100 Pa [64].
2. *Decrease the radical/ion flux:* This is the source of the dissolved hydrogen, if it could be reduced the supersaturation ratio would decrease. However, if there would be a way to significantly and consistently reduce the ion flux on the divertor there would not be a need for an LM divertor.
3. *Increase the impurity/oxide layer of the LM:* In Sect. 4.3 it was shown that oxides could form a barrier for hydrogen to reach the LM. However, these additional impurities which will eventually be eroded and increase the Z_{eff} of the plasma, leading to increased radiation [78]. Furthermore, the added oxygen can lead to unwanted oxidation of other in-vessel components. The eroded material could also increase the sputtering yield, since its atomic number is higher than the plasma species.
4. *Increase the liquid metal temperature:* As shown in Figs. 2, 5 and 6, to achieve a low supersaturation ratio requires a high temperature by increasing the solubility of the H in the liquid metal. However, the temperatures required would have to be high enough that evaporation would become significant. Instead of having erosion in the form of droplets, Sn vapour would now dominate. Furthermore, there will be regions outside

the strike point where the temperature is lower. Therefore, this is also not an acceptable solution.

5. *Reduce the pore size of the CPS:* A bubble can only grow when its radius is larger than r_{crit}, defined in Eq. (28). Additionally, the collapse of a bubble only leads to droplet ejection when $r_b > r^*$, as explained in Sect. 2.6. Furthermore, this would reduce the bubble size and by extension the size of the ejected droplets, see Eq. (29). The pore size of the sintered disc and crucible is already micron-sized. It will be difficult to find a manufacturing technique that could significantly improve this. Even if they could be made, a CPS with nano pores will give rise to numerous other challenges like increased brittleness and wetting of the CPS. These challenges were already encountered here with the sweating of Sn droplets and the crack in the sintered disc. Hence, reducing the pore size will reduce droplet ejection, but is not sufficient to prevent it completely.
6. *Fragmentation of bubbles:* This would, similar to the solution above, limit the bubble size. A possible way to do this is by mixing the liquid, this would require a flowing LMD, which will be discussed in more detail below. Another option could be by sending shock waves to the LMD, which can generate a train of expansion and compression waves that fragment the bubble [79]. This does, however, introduce more mechanical stress and potentially fatigue, which could significantly reduce the life-time of the solid components. Furthermore, there are now more bubbles and the total bubble surface area is increased, which enhances bubble growth through diffusion. Therefore, if not applied properly, this could lead to more severe droplet ejection [79].
7. *Divertor designs with no direct line of sight to the plasma:* Concepts such as this include the vapour box [80] or Super-X divertor [81] as has been implemented in the MAST-U tokamak [82]. In such a scenario the ejected droplets could not travel directly into the plasma core, but they could still ablate and the Sn ions be transported via the SOL into the core. Additionally, some droplets will be ejected to a place where they are in direct line of sight with the main plasma. From there, droplets could reach the plasma in a second ejection event. The droplet will, however, now be located in the private flux region, outer scrape-off layer (SOL) or another region where the ion flux is lower. This might provide enough time to remove the droplet by absorbing it into an empty CPS. In contrast to current designs [4, 5], this would require substantial modifications to the baseline design of the divertor, and would make it significantly more complex.
8. *An upper LMD:* Bubbles rise to the surface before they collapse due to the buoyancy force. Placing the divertor at the top of the reactor, rather than at the bottom, enhances the transport of bubbles away from the PFS. At the side of the CPS that is not facing the plasma, one could degas the liquid metal by promoting bubble collapse. However, if there still are droplets (although less) or the liquid is no longer confined in the CPS due to another instability, the metals could reach the core more easily due to gravity. Such a solution also requires the gas bubbles to be transported fast enough through the tiny pores of the CPS. Additionally, the channels could become blocked with bubbles, preventing capillary refilling of the surface, or a gas pocket could form between the LM and the cooling structures. These issues would hinder the flow of LM, reducing its replenishment and cooling efficiency.
9. *A flowing LMD:* Reaching supersaturation takes time, something which is neglected in the steady-state analysis in Sect. 2. This time could be used to refresh the liquid metal through active flow, similar to [4]. An estimation of the minimal velocity that a liquid should have in a flowing LM divertor can be determined using:

$$v_{Min} = \frac{\Gamma_{\mathrm{H},tot} l}{Sc_{\mathrm{H}} h N_A} \tag{32}$$

with $\Gamma_{\mathrm{H},tot}$ the total hydrogen flux (gas, ion and radicals) arriving at the liquid metal. Additionally, h the height of the LM layer on top of the substrate, l the total distance the liquid metal needs to flow and c_H the steady-state molarity of hydrogen in an LM, which can be determined using:

$$c_{\mathrm{H},g} = x_{\mathrm{H},g} \frac{\rho}{M} \tag{33}$$

The assumption for Γ_{H}, S, h and S can be found in Table 4 for a best-case and worst-case scenario and $x_{\mathrm{H},g}$ can be calculated using Eq. (7). The resulting flow velocities can be found in Fig. 20. For Sn, large flow velocities or high temperatures are needed to prevent droplet ejection altogether. Still, at 800 °C the

Table 4 Best and worst-case scenarios for an LMD

	Best-case	Worst-case
$\Gamma_{\mathrm{H},tot}$ [at m^{-2} s^{-1}]	10^{20}	10^{23}
S [−]	5	5
h [mm]	1	0.1 [77]
l [m]	1	1 [1]
p_{H_2} [Pa]	100	1 [64]

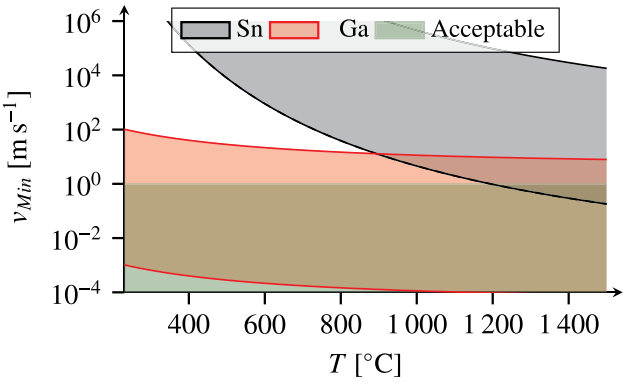

Fig. 20 Minimum flow speed before the droplets would be ejected in a flowing LMD. The upper and lower lines are based on the best and worst-case scenarios. The green region indicates an acceptable limit for a flowing LM divertor concept

velocities required would be in the order of kms^{-1} even in the best-case scenario, and thus this option seem unrealistic. Of course, this is a crude approximation and perhaps the numbers used for the assumptions are still too pessimistic.

10. *Use another metal than Sn, examples could Li, Ga, or an alloy:* Li has a lower atomic mass than Sn and thus more lithium can be allowed in the plasma core. Furthermore, the high affinity of lithium with hydrogen prevents hydrogen from dissolving in the metal and thus the ejection of droplets. The hydrogen solubility in gallium is significantly higher compared to tin [37–39, 76]. This gives more time before the supersaturation ratio is reached, and thus a more reasonable flow speed in a flowing LM divertor is required. It is important to note here that both metals have other disadvantages that need to be tackled. The high reactivity of lithium makes it a safety risk, and the high tritium retention [26, 28] increases the tritium inventory above the set limit [5, 83]. There are technologies being developed to separate hydrogen isotopes from liquid lithium in the divertor [84]. However, tritium also retains through co-deposits on the first wall, where it is more difficult to remove [28, 85]. Furthermore, it remains uncertain how long tritium would be trapped in the purification system, which influences the tritium stock required to start a fusion reactor. Gallium is corrosive to structural materials i.e. steels [86–89].

Some Remarks About the Validity of the Model

In the model of Sect. 2, no interaction is assumed between the plasma, free radicals, and the gas. They are taken as independent input variables in the equations. Furthermore, the hydrogen solubility for Sn is only experimentally verified between $T = 1000-1300$ °C in 1944 [37, 76] and recently in 2024, but only at the melting point [38]. The latter only found a minimum value of $x_{H/Sn} < 1$ ppb. This makes the extrapolation to the 300–500 °C used in this work uncertain. Furthermore, it has been assumed that the liquid can be confined in a region with the size of the pores, but the liquid layer on the surface of the CPS might be thicker than that. This could have implications on the stability of the KH and RT instabilities discussed in Sect. 2.1, but also on the size that gas bubbles can have.

Conclusions

The ejection of droplets was identified as a potential showstopper for the use of tin as a plasma-facing component for a nuclear fusion reactor, due to the unavoidable formation of gas bubbles. This mechanism can be summarized as follows: If exposed to a hydrogen plasma, hydrogen in the form of free radicals and ions get dissolved in tin. The solubility limit in tin is low (< 1 ppb) at the melting point, and therefore it is energetically more favourable for the dissolved gas to nucleate and form bubbles. In a liquid metal divertor, the liquid is confined using a capillary porous structure, which has pre-existing gas cavities or irregularities formed during manufacturing, which may provide a nucleation site. The bubbles can grow through diffusion into the bubble from dissolved hydrogen near the bubble and rise towards the surface until it collapses. Due to inertial and surface tension forces, a Worthington jet is formed, this jet becomes thinner and droplets are formed due to the Rayleigh-Plateau instability. If the pores are smaller than the critical bubble radius (r_{crit}), gas bubbles would shrink and droplet ejection could be avoided. This is because at the critical radius, the pressure inside a gas bubble is in balance with the surface tension. In this work, we outline a theory that describes under what conditions of flux, temperature, and pore size bubbles should be expected to form and grow, resulting in droplet ejection, for different liquid metals. The theory predicts that this behaviour should be general to all liquid metals that do not strongly chemically react with hydrogen, and that above a certain temperature bubbling should be suppressed at a given ratio of radical to gas or ion to gas pressures. However, according to the theory, the required radius is too small to be achieved with any known manufacturing technique, at least while the temperature is low enough so that evaporation does not become significant. In this work, five hypotheses based on the theory described above were experimentally tested.

- A shadowgraph set-up was added to nano-PSI, where with high-frequency imaging the collapse of a hydrogen bubble was observed, confirming the hypothesis that this is the driving force for droplet ejection.
- Multiple manufacturing techniques were used to make tungsten CPSs, in order to suppress droplet ejection.

These were: two types of braids, a felt, two types of sintering, and 3D printing. All of these were filled with Sn and exposed to hydrogen plasma using nano-PSI. Although significant differences in performance were observed, with the least ejection in the felts and the most for the braids, no target was ejection-free. The theory indicated that smaller pores would reduce erosion, which implied that the sintered disc would show the best performance. However, tin droplets sweated from this CPS leading to the formation of a free surface layer, from which droplets would be ejected.

- Different post-transition metals (tin, indium, gallium, bismuth, and lead) were also exposed to nano-PSI hydrogen plasmas. They were observed to eject droplets as predicted by the theory. However, the erosion from bismuth and lead was clearly less than that of the other two, possibly due to the higher mass density, which reduces the likelihood that the droplets could leave the cup. In addition, the formation of an oxide layer on top of the liquid metals increased the incubation time before ejection started. As a result, this limited our ability to make quantitative comparisons. Besides the post-transition metals, three different alkali metals were tested (lithium, sodium, and potassium). During these tests, no droplet ejection was observed for the alkali metals. However, the last two exposures were terminated prematurely due to overheating of the liquid metal. This can also be explained by the theory, since the hydrogen would react with these metals rather than dissolve into them.
- Hydrogen radicals alone are already sufficient to cause droplet ejection in tin and gallium.
- Droplet ejection can be suppressed by increasing the temperature of the liquid, in line with the model prediction. However, this was at a lower temperature than predicted.

On the basis of the theory and with the experience of the experiment, possible solutions have been identified for droplet ejection. However, none of them can be implemented without a major design change in the currently proposed liquid metal divertor concepts for EU-DEMO. Two promising options are given to still make a liquid metal divertor viable. The first is to prevent droplets from reaching the main plasma directly and capture them before a second ejection event can occur. The second is to change from tin to lithium, gallium, or an alloy as a plasma-facing component. Both solutions are not ideal and will undoubtedly result in other challenges that are not addressed in the paper.

Appendix A. Temperature Dependent Material Properties

See Table 5.

Table 5 Relevant material properties for the used post-transition metals, as function of T [K]. Values of the standard enthalpy and entropy of the formation of hydrogen dissolved in the LM have the same source and are used in Eq. (9). The values for ΔH_S° and ΔS_S° were not obtained for Bi. The surface tension is given for the melting point (T_m)

	T_{melt} [°C]	$\Delta G^\circ_{H_2}$ [J mol^{-1}]	γ [mN m^{-1}]	μ [mPa s]
Li	180.5	–	$398 - 0.147T$	$10^3 \exp\left(-4.164 - 0.6374 \ln T + \frac{292.1}{T}\right)$
Ga	29.8	$1.58 \times 10^4 + 5.4T$	$708 - 0.066(T - 29.8)$	$10^{\frac{204.03}{T} - 0.4465}$
In	156.6	$1.19 \times 10^4 + 9.3T$	$558 - 8 \times 10^{-3}(T - 425)$	$10^{\frac{272.06}{T} - 0.3621}$
Sn	231.9	$1.15 \times 10^5 + 17.9T$	$606 - 0.091T$	$0.3908 \exp\left(\frac{790.7}{T}\right)$
Pb	327.5	$4.6 \times 10^4 - 17.43T$	$444.2 - 0.094(T - 600.61)$	$10^{\frac{440.1}{T} - 0.3134}$
Bi	271.3	–	$404.5 - 0.0492T$	$0.296 \exp\left(\frac{8.45 \times 10^3}{R_g T}\right)$

	ρ [kg m^{-3}]	D [m^2 s^{-1}]	Sources
Li	$278.5 - 0.04657T + 274.6\left(1 - \frac{T}{3500}\right)^{0.467}$		[90]
Ga	$6077 - 0.611(T - 302.914)$	$8.63 \times 10^{-8} \exp\left(-\frac{2 \times 10^4}{R_g T}\right)$	[39, 91, 92]
In	$7022 - 0.762(T - 429.748)$	$1.32 \times 10^{-7} \exp\left(-\frac{25.7 \times 10^3}{R_g T}\right)$	[39, 92, 93]
Sn	$6979 - 0.652(T - 505.08)$	$2.33 \times 10^{-7} \exp\left(-\frac{11980}{R_g T}\right)$	[37, 76]
Pb	$1.113 \times 10^4 - 1.4 \times 10^{-6} T$		[40, 94–96]
Bi	$10665 - 1.182T$		[97–99]

Appendix B. Mass of Added Liquid Min the Cups

See Table 6.

Table 6 Mass and volume of the added LM, during the various tests

Metal	Test	Volume [cm^3] $\pm 5mm^3$	Mass [g] ±5 mg
Sn	Comparison CPSs	0.78	5.50
Ga	Round 1	1.20	7.08
In	Round 1	1.20	8.55
Sn	Round 1	1.18	8.45
Pb	Round 1	1.20	13.71
Bi	Round 1	1.21	11.83
Li	Alkali metal	1.22	0.65
Na	Alkali metal	1.26	1.22
Pb	Alkali metal	1.25	1.07
Ga	Round 4 and radical source	1.97	11.61
In	Round 4	1.99	14.11
Sn	Round 4 and radical source	2.00	14.17
Pb	Round 4	1.63	18.60
Bi	Round 4	1.23	11.95

Acknowledgements This work has been carried out within the framework of the EUROfusion Consortium, funded by the European Union via the Euratom Research and Training Programme (Grant Agreement No 101052200 - EUROfusion). Views and opinions expressed are however those of the author(s) only and do not necessarily reflect those of the European Union or the European Commission. Neither the European Union not the European Commission can be held responsible for them.

Author Contributions JGAS: wrote the main manuscript JGAS, AM, SR, EM, MI and DH: prepared targets JGAS, RSA and JWMV: prepare setup and conduct experiments JGAS, AM, MM, RSA, TWM: reviewed the manuscript JGAS, MM: data analysis TWM: supervision.

Data Availability No datasets were generated or analysed during the current study

Declarations

Competing interests The authors declare no competing interests.

References

1. J. You, G. Mazzone, E. Visca, H. Greuner, M. Fursdon, Y. Addab, C. Bachmann, T. Barrett, U. Bonavolontà, B. Böswirth, F. Castrovinci, C. Carelli, D. Coccorese, R. Coppola, F. Crescenzi, G. Di Gironimo, P. Di Maio, G. Di Mambro, F. Domptail, D. Dongiovanni, G. Dose, D. Flammini, L. Forest, P. Frosi, F. Gallay, B. Ghidersa, C. Harrington, K. Hunger, V. Imbriani, M. Li, A. Lukenskas, A. Maffucci, N. Mantel, D. Marzullo, T. Minniti, A. Müller, S. Noce, M. Porfiri, A. Quartararo, M. Richou, S. Roccella, D. Terentyev, A. Tincani, E. Vallone, S. Ventre, R. Villari, F. Villone, C. Vorpahl, K. Zhang, Divertor of the European DEMO: engineering and technologies for power exhaust. Fusion Eng. Des. **175**, 113010 (2022)
2. G. Pintsuk, Tungsten as a plasma-facing material, in *Comprehensive Nuclear Materials*, vol 1–5 (Elsevier, 2012), pp. 551–581. https://doi.org/10.1016/B978-0-08-056033-5.00118-X
3. G.G. van Eden, V. Kvon, M.C.M. van de Sanden, T.W. Morgan, Oscillatory vapour shielding of liquid metal walls in nuclear fusion devices. Nat. Commun. **8**(1), 192 (2017). https://doi.org/10.1038/s41467-017-00288-y
4. S. Roccella, G. Dose, R. de Luca, M. Iafrati, A. Mancini, G. Mazzitelli, CPS based liquid metal divertor target for EU-DEMO. J. Fusion Energ. **39**(6), 462–468 (2020). https://doi.org/10.1007/s10894-020-00263-4
5. P. Rindt, J.L. van den Eijnden, T.W. Morgan, N.J. Lopes Cardozo, Conceptual design of a liquid-metal divertor for the European DEMO. Fusion Eng. Des. **173**, 112812 (2021). https://doi.org/10.1016/j.fusengdes.2021.112812
6. W. Ou, F. Brochard, T.W. Morgan, Bubble formation in liquid Sn under different plasma loading conditions leading to droplet ejection. Nucl. Fusion **61**(6), 066030 (2021). https://doi.org/10.1088/1741-4326/abf9e0
7. A. Manhard, T. Schwarz-Selinger, M. Balden, T. Dürbeck, H. Maier, R. Neu, Deuterium retention in solid and liquid tin after low-temperature plasma exposure. Nucl. Fusion **60**(10), 106007 (2020). https://doi.org/10.1088/1741-4326/aba801
8. J. Scholte, M. Iafrati, S. Lam, B. Tyburska-Pueschel, M. Riepen, F. Brochard, M. Vissers, T. Morgan, Reducing tin droplet ejection from capillary porous structures under hydrogen plasma exposure in Magnum-PSI. Nucl. Mater. Energy **34**, 101315 (2023). https://doi.org/10.1016/j.nme.2022.101315
9. A. Manhard, Stabilization of liquid tin surfaces under D plasma irradiation by a capillary porous system. Nucl. Mater. Energy **40**(December 2023), 101696 (2024). https://doi.org/10.1016/j.nme.2024.101696
10. J. Bramble, C. Moynihan, S. Stemmley, J. Stermer, J. Robertson, N. Weissburg, D.N. Ruzic, Ejection of molten tin in the presence of a hydrogen plasma. Fusion Eng. Des. **207**(May), 114622 (2024). https://doi.org/10.1016/j.fusengdes.2024.114622
11. J. Scholte, M. Balden, D. Brida, J. Cecrdle, R. Dux, S. Elgeti, M. Faitsch, A. Herrmann, J. Horacek, K. Hunger, K. Krieger, A. Manhard, P. de Marné, V. Rohde, T. Morgan, Performance of a liquid Sn divertor target during ASDEX upgrade L-mode and H-mode operation. Nucl. Mater. Energy **37**(September), 101522 (2023). https://doi.org/10.1016/j.nme.2023.101522
12. F.L. Tabarés, E. Oyarzabal, A.B. Martin-Rojo, D. Tafalla, A. De Castro, A. Soleto, Reactor plasma facing component designs based on liquid metal concepts supported in porous systems. Nucl. Fusion (2016). https://doi.org/10.1088/0029-5515/57/1/016029

13. D.G. Whyte, T.E. Evans, C.P. Wong, W.P. West, R. Bastasz, J.P. Allain, J.N. Brooks, Experimental observations of lithium as a plasma-facing surface in the DIII-D tokamak divertor. Fusion Eng. Des. **72**(1–3 SPEC. ISS.), 133–147 (2004). https://doi.org/10.1016/j.fusengdes.2004.07.014
14. G.Z. Zuo, J. Ren, J.S. Hu, Z. Sun, Q.X. Yang, J.G. Li, L.E. Zakharov, D.N. Ruzic, Liquid lithium surface control and its effect on plasma performance in the HT-7 tokamak. Fusion Eng. Des. **89**(12), 2845–2852 (2014). https://doi.org/10.1016/j.fusengdes.2014.05.020
15. B. Bazylev, G. Janeschitz, I. Landman, A. Loarte, N.S. Klimov, V.L. Podkovyrovd, V.M. Safronov, Experimental and theoretical investigation of droplet emission from tungsten melt layer. Fusion Eng. Des. **84**(2–6), 441–445 (2009). https://doi.org/10.1016/j.fusengdes.2008.12.123
16. B. Bazylev, I. Landman, A. Loarte, N.S. Klimov, V.L. Podkovyrov, V.M. Safronov, Experiments and modeling of droplet emission from tungsten under transient heat loads. Phys. Scr. (2009). https://doi.org/10.1088/0031-8949/2009/T138/014061
17. V.A. Evtikhin, I.E. Lyublinski, A.V. Vertkov, V.G. Belan, I.K. Konkashbaev, L.B. Nikandrov, Calculation and experimental investigation of fusion reactor divertor plate and first wall protection by capillary-pore systems with lithium. J. Nucl. Mater. **271–272**, 396–400 (1999). https://doi.org/10.1016/S0022-3115(98)00793-4
18. M.A. Jaworski, T. Abrams, J.P. Allain, M.G. Bell, R.E. Bell, A. Diallo, T.K. Gray, S.P. Gerhardt, R. Kaita, H.W. Kugel, B.P. Leblanc, R. Maingi, A.G. McLean, J. Menard, R. Nygren, M. Ono, M. Podesta, A.L. Roquemore, S.A. Sabbagh, F. Scotti, C.H. Skinner, V.A. Soukhanovskii, D.P. Stotler, Liquid lithium divertor characteristics and plasma-material interactions in NSTX high-performance plasmas. Nucl. Fusion (2013). https://doi.org/10.1088/0029-5515/53/8/083032
19. G. Miloshevsky, A. Hassanein, Modelling of Kelvin-Helmholtz instability and splashing of melt layers from plasma-facing components in tokamaks under plasma impact. Nucl. Fusion **50**(11), 115005 (2010). https://doi.org/10.1088/0029-5515/50/11/115005
20. T. Morgan, A. Vertkov, K. Bystrov, I. Lyublinski, J. Genuit, G. Mazzitelli, Power handling of a liquid-metal based CPS structure under high steady-state heat and particle fluxes. Nucl. Mater. Energy **12**, 210–215 (2017). https://doi.org/10.1016/j.nme.2017.01.017
21. Y. Hamana, N. Shirai, K. Sasaki, Mechanism of droplet ejection from liquid gallium interacting with inductively coupled hydrogen plasma. J. Phys. D Appl. Phys. (2023). https://doi.org/10.1088/1361-6463/acf227
22. J. Miyazawa, T. Goto, Y. Hamaji, M.I. Kobayashi, Novel features of the helical volumetric neutron source FFHR-b2. Nucl. Fusion (2021). https://doi.org/10.1088/1741-4326/ac25bd
23. K. Tamura, J. Miyazawa, S. Masuzaki, M. Tokitani, Y. Hamaji, H. Toyoda, Bubbling phenomenon of liquidized Sn–Bi–Li–Er alloy under hydrogen plasma exposure. Jpn. J. Appl. Phys. (2022). https://doi.org/10.35848/1347-4065/ac92b1
24. D. Shefer, A. Nikipelov, M. van de Kerkhof, Z. Marvi, V. Banine, J. Beckers, The impact of hydrogen plasma on the structure and morphology of tin and lead micrometer sized particles. J. Phys. D Appl. Phys. (2023). https://doi.org/10.1088/1361-6463/acb3d9
25. G. Mazzitelli, M.L. Apicella, M. Iafrati, G. Apruzzese, F. Bombarda, F. Crescenzi, L. Gabellieri, A. Mancini, M. Marinucci, A. Romano, Experiments on the Frascati Tokamak Upgrade with a liquid tin limiter. Nucl. Fusion **59**(9), 096004 (2019). https://doi.org/10.1088/1741-4326/ab1d70
26. M. Baldwin, R. Doerner, S. Luckhardt, R. Conn, Deuterium retention in liquid lithium. Nucl. Fusion **42**(11), 1318–1323 (2002). https://doi.org/10.1088/0029-5515/42/11/305
27. M. Christenson, D. Panici, C. Moynihan, J. Wendeborn, J. Anderson, D.N. Ruzic, A study on hydrogen absorption and dissolution in liquid lithium. Nucl. Fusion (2019). https://doi.org/10.1088/1741-4326/aaf587
28. M. Morbey, J. Gonzalez, W. Arnoldbik, B. Tyburska-Pueschel, T. Morgan, Deuterium retention in co-deposition with lithium in Magnum-PSI: experimental analysis and comparison with SOLPS-ITER. Nucl. Fusion (2024). https://doi.org/10.1088/1741-4326/ad4614
29. R. Dejarnac, J. Horacek, M. Hron, M. Jerab, J. Adamek, S. Atikukke, P. Barton, J. Cavalier, J. Cecrdle, M. Dimitrova, E. Gauthier, M. Iafrati, M. Imrisek, A. Marin Roldan, G. Mazzitelli, D. Naydenkova, A. Prishvitcyn, M. Tomes, D. Tskhakaya, G. Van Oost, J. Varju, P. Veis, A. Vertkov, P. Vondracek, V. Weinzettl, Overview of power exhaust experiments in the COMPASS divertor with liquid metals. Nucl. Mater. Energy **25**, 100801 (2020). https://doi.org/10.1016/j.nme.2020.100801
30. J.S. Hu, G.Z. Zuo, L. Li, D.H. Zhang, H.L. Bi, Z.B. Ye, J.H. Pan, S.Y. Dai, X.C. Meng, Z. Sun, M. Ono, Y. Hirooka, D.N. Ruzic, Recent progress in the development of liquid metal plasma facing components for magnetic fusion devices. Nucl. Mater. Energy (2024). https://doi.org/10.1016/j.nme.2024.101776
31. A. Pisarev, I. Arkhipov, Y. Babich, M. Berdnikova, Y. Gasparyan, K. Gutorov, S. Grashin, V. Efimov, M. Isaenkova, S. Krat, O. Krymskaya, V. Kurnaev, T. Stepanova, E. Vovchenko, I. Vizgalov, M. Zibrov, Post-mortem analyses of gap facing surfaces of tungsten tiles of T-10 ring limiter. Fusion Eng. Des. **162**(March 2020), 112105 (2021). https://doi.org/10.1016/j.fusengdes.2020.112105
32. A.F.H. Kaplan, J. Powell, Spatter in laser welding. J. Laser Appl. (2011). https://doi.org/10.2351/1.3597830
33. G. Miloshevsky, A. Hassanein, Splashing and boiling mechanisms of melt layer losses of PFCs during plasma instabilities. J. Nucl. Mater. **438**(SUPPL), 155–159 (2013). https://doi.org/10.1016/j.jnucmat.2013.01.024
34. K. Tamaru, The thermal decomposition of tin hydride. J. Phys. Chem. **60**(5), 610–612 (1956)
35. S. Peillon, G. Dougniaux, M. Payet, E. Bernard, G. Pieters, S. Feuillastre, S. Garcia-Argote, F. Gensdarmes, C. Arnas, F. Miserque, N. Herlin-Boime, C. Grisolia, O. Pluchery, Dust sampling in WEST and tritium retention in tokamak-relevant tungsten particles. Nucl. Mater. Energy **24**(August), 100781 (2020). https://doi.org/10.1016/j.nme.2020.100781
36. T. Tanabe, Y. Furuyama, S. Imoto, Hydrogen ion driven permeation through metals. J. Nucl. Mater. **145–147**(1), 305–308 (1987). https://doi.org/10.1016/0022-3115(87)90349-7
37. M.B. Bever, C.F. Floe, Solubility of hydrogen in molten copper-tin alloys. MET Technol. **11**(3), 1–11 (1944)
38. V. Nemanič, M. Žumer, J. Zavašnik, U. Cvelbar, Hydrogen interaction with solid and liquid tin. J. Nucl. Mater. (2024). https://doi.org/10.1016/j.jnucmat.2023.154771
39. N.D. Deveau, P.S. Yen, R. Datta, Evaluation of hydrogen sorption and permeation parameters in liquid metal membranes via Sieverts' apparatus. Int. J. Hydrogen Energy **43**(41), 19075–19090 (2018). https://doi.org/10.1016/j.ijhydene.2018.08.101
40. M. Hoch, The solubility of hydrogen, deuterium and tritium in liquid lead-lithium alloys. J. Nucl. Mater. **120**(1), 102–112 (1984). https://doi.org/10.1016/0022-3115(84)90177-6
41. M.A. Pick, K. Sonnenberg, A model for atomic hydrogen-metal interactions—application to recycling, recombination and permeation. J. Nucl. Mater. **131**(2–3), 208–220 (1985). https://doi.org/10.1016/0022-3115(85)90459-3
42. O. Ogorodnikova, Comparison of hydrogen gas-, atom- and ion-metal interactions. J. Nucl. Mater. **277**(2–3), 130–142 (2000). https://doi.org/10.1016/S0022-3115(99)00206-8

43. S. Markelj, O.V. Ogorodnikova, P. Pelicon, T. Schwarz-Selinger, I. Čadež, Temperature dependence of D atom adsorption on polycrystalline tungsten. Appl. Surf. Sci. **282**, 478–486 (2013). https://doi.org/10.1016/j.apsusc.2013.05.157
44. E.A. Hodille, S. Markelj, M. Pecovnik, M. Ajmalghan, Z.A. Piazza, Y. Ferro, T. Schwarz-Selinger, C. Grisolia, Kinetic model for hydrogen absorption in tungsten with coverage dependent surface mechanisms. Nucl. Fusion (2020). https://doi.org/10.1088/1741-4326/aba454
45. S.C. Wang, M. van Kampen, T.W. Morgan, Promotion of plasma-induced deuterium uptake in ruthenium films by monolayer-thick tin layers. ACS Appl. Mater. Interfaces **5**, 10 (2023). https://doi.org/10.1021/acsami.3c11245
46. C. Onwudinanti, I. Tranca, T. Morgan, S. Tao, Tin, the enabler-hydrogen diffusion into ruthenium. Nanomaterials **9**(1), 1–18 (2019). https://doi.org/10.3390/nano9010129
47. W.M. T. A. T. T.W. Haynes, *CRC Handbook of Chemistry and Physics*, 95th Ed (CRC Press, Hoboken, 2014). LK - https://tue.on.worldcat.org/oclc/908078665, http://search.ebscohost.com/login.aspx?direct=true&scope=site &db=nlebk &db=nlabk &AN=1631986, http://www.hbcpnetbase.com
48. M.J. de Graaf, R. Severens, R.P. Dahiya, M. van de Sanden, D.C. Schram, Anomalous fast recombination in hydrogen plasmas involving rovibrational excitation. Phys. Rev. E **48**(3), 2098–2102 (1993). https://doi.org/10.1103/PhysRevE.48.2098
49. P.S. Szabo, D. Weichselbaum, H. Biber, C. Cupak, A. Mutzke, R.A. Wilhelm, F. Aumayr, Graphical user interface for SDTrimSP to simulate sputtering, ion implantation and the dynamic effects of ion irradiation. Nucl. Instrum. Methods Phys. Res. Sect. B **522**(May), 47–53 (2022). https://doi.org/10.1016/j.nimb.2022.04.008.
50. J.F. Ziegler, M.D. Ziegler, J.P. Biersack, SRIM—the stopping and range of ions in matter (2010). Nucl. Instrum. Methods Phys. Res. Sect. B **268**(11–12), 1818–1823 (2010). https://doi.org/10.1016/j.nimb.2010.02.091
51. G. Liger-Belair, G. Polidori, P. Jeandet, Recent advances in the science of champagne bubbles. Chem. Soc. Rev. **37**(11), 2490–2511 (2008). https://doi.org/10.1039/b717798b
52. G. Liger-Belair, Effervescence in champagne and sparkling wines: from grape harvest to bubble rise. Eur. Phys. J. Spec. Top. **226**(1), 3–116 (2017). https://doi.org/10.1140/epjst/e2017-02678-7
53. G. Liger-Belair, Carbon dioxide in bottled carbonated waters and subsequent bubble nucleation under standard tasting condition. J. Agric. Food Chem. **67**(16), 4560–4567 (2019). https://doi.org/10.1021/acs.jafc.9b00155
54. S. Jones, G. Evans, K. Galvin, Bubble nucleation from gas cavities—a review. Adv. Colloid Interface. Sci. **80**(1), 27–50 (1999). https://doi.org/10.1016/S0001-8686(98)00074-8
55. K.W. Kolasinski, Bubbles: a review of their relationship to the formation of thin films and porous materials. Open Mater. Sci. **1**(1), 49–60 (2014). https://doi.org/10.2478/mesbi-2014-0003
56. T.S. Kuntzleman, R. Johnson, Probing the mechanism of bubble nucleation in and the effect of atmospheric pressure on the candy-cola soda geyser. J. Chem. Educ. **97**(4), 980–985 (2020). https://doi.org/10.1021/acs.jchemed.9b01177
57. T. Séon, G. Liger-Belair, Effervescence in champagne and sparkling wines: from bubble bursting to droplet evaporation. Eur. Phys. J. Spec. Top. **226**(1), 117–156 (2017). https://doi.org/10.1140/epjst/e2017-02679-6
58. A.M. Worthington, R.S. Cole, V. Impact with a liquid surface, studied by the aid of instantaneous photography. Philos. Trans. R. Soc. Lond. Ser. A Contain. Pap. Math. Phys. Charact. **189**, 137–148 (1897). https://doi.org/10.1098/rsta.1897.0005
59. J.S. Lee, B.M. Weon, S.J. Park, J.H. Je, K. Fezzaa, W.K. Lee, Size limits the formation of liquid jets during bubble bursting. Nat. Commun. **2**(1), 367 (2011). https://doi.org/10.1038/ncomms1369
60. S.C. Wang, R.M. van der Horst, M. van Kampen, T.W. Morgan, Application of a dual-thermopile radical probe to expanding hydrogen plasmas. Plasma Sources Sci. Technol. **31**(8), 085011 (2022). https://doi.org/10.1088/1361-6595/ac71c3
61. H. van Eck, G. Akkermans, S. Alonso van der Westen, D. Aussems, M. van Berkel, S. Brons, I. Classen, H. van der Meiden, T. Morgan, M. van de Pol, J. Scholten, J. Vernimmen, E. Vos, M. de Baar, High-fluence and high-flux performance characteristics of the superconducting Magnum-PSI linear plasma facility. Fusion Eng. Des. **142**(April), 26–32 (2019). https://doi.org/10.1016/j.fusengdes.2019.04.020
62. R. Pitts, X. Bonnin, F. Escourbiac, H. Frerichs, J. Gunn, T. Hirai, A. Kukushkin, E. Kaveeva, M. Miller, D. Moulton, V. Rozhansky, I. Senichenkov, E. Sytova, O. Schmitz, P. Stangeby, G. De Temmerman, I. Veselova, S. Wiesen, Physics basis for the first ITER tungsten divertor. Nucl. Mater. Energy **20**, 100696 (2019). https://doi.org/10.1016/j.nme.2019.100696
63. S.Q. Korving, G.T. Huijsmans, J.S. Park, A. Loarte, Development of the neutral model in the nonlinear MHD code JOREK: application to e × B drifts in ITER PFPO-1 plasmas. Phys. Plasmas (2023). https://doi.org/10.1063/5.0135318
64. F. Subba, D.P. Coster, M. Moscheni, M. Siccinio, SOLPS-ITER modeling of divertor scenarios for EU-DEMO. Nucl. Fusion (2021). https://doi.org/10.1088/1741-4326/ac1c85
65. Y. Zou, X. An, R. Zou, Investigation of densification behavior of tungsten powders during hot isostatic pressing with a 3D multi-particle FEM approach. Powder Technol. **361**, 297–305 (2020). https://doi.org/10.1016/j.powtec.2019.08.014
66. E. Oyarzabal, F. Tabarés, M. Liniers, D. Alegre, D. Tafalla, K. McCarthy, A. de Castro, T. Morgan, J. Scholte, M. Iafrati, E. de la Cal, I. Voldimer, E. Ascasíbar, A. Soleto, Comparative study of different Sn wetted W CPSs exposed to NBI fluxes in the OLMAT facility. Fusion Eng. Des. **190**(October 2022), 113711 (2023). https://doi.org/10.1016/j.fusengdes.2023.113711
67. P. Rindt, J. Mata González, P. Hoogerhuis, P. van den Bosch, M. van Maris, D. Terentyev, C. Yin, M. Wirtz, N. Lopes Cardozo, J. van Dommelen, T. Morgan, Using 3D-printed tungsten to optimize liquid metal divertor targets for flow and thermal stresses. Nucl. Fusion **59**(5), 054001 (2019). https://doi.org/10.1088/1741-4326/ab0a76
68. J. Scholte, M. Balden, B. Böswirth, S. Elgeti, H. Greuner, A. Herrmann, K. Hunger, K. Krieger, P. Leitenstern, A. Manhard, R. Neu, R. van Schaik, V. Rohde, I. Zammuto, T. Morgan, Design and GLADIS testing of a liquid tin divertor module prior to exposure in ASDEX Upgrade. Nucl. Mater. Energy **37**, 101528 (2023). https://doi.org/10.1016/j.nme.2023.101528
69. uhv.htmModel 102916 2" Sample Stage and 102915 2" 1200°C O2 Heater Dock Assembly from HeatWave labs. https://www.cathode.com/h_uhv.htm. Accessed 24 Sept 2024
70. W. Zheng, A. Gallagher, Hydrogen dissociation on high-temperature tungsten. Surf. Sci. **600**(10), 2207–2213 (2006). https://doi.org/10.1016/j.susc.2006.03.032
71. P.D. Desai, T.K. Chu, H.M. James, C.Y. Ho, Electrical resistivity of selected elements. J. Phys. Chem. Ref. Data **13**(4), 1069–1096 (1984). https://doi.org/10.1063/1.555723
72. D. Mous, W. Fokker, R. Van Den Broek, R. Koopmans, C.B. Ramsey, R. Hedges, An ion source for the HVEE 14 C isotope ratio mass spectrometer for biomedical applications. Radiocarbon **40**(1), 283–288 (1997). https://doi.org/10.1017/S0033822200018154
73. N. Barradas, C. Jeynes, Advanced physics and algorithms in the IBA DataFurnace. Nucl. Instrum. Methods Phys. Res. Sect. B **266**(8), 1875–1879 (2008). https://doi.org/10.1016/j.nimb.2007.10.044

74. M. Mayer, RESOLNRA: a new program for optimizing the achievable depth resolution of ion beam analysis methods. Nucl. Instrum. Methods Phys. Res. Sect. B **266**(8), 1852–1857 (2008). https://doi.org/10.1016/j.nimb.2007.11.071
75. A. Vesel, M. Mozetič, M. Balat-Pichelin, Sequential oxidation and reduction of tungsten/tungsten oxide. Thin Solid Films **591**, 174–181 (2015). https://doi.org/10.1016/j.tsf.2015.02.019
76. P.W. Humrickhouse, An equation of state and compendium of thermophysical properties of liquid tin, a prospective plasma-facing material. IEEE Trans. Plasma Sci. **47**(7), 3374–3379 (2019). https://doi.org/10.1109/TPS.2019.2919034
77. L.E. Zakharov, W. Blanchard, R. Kaita, H. Kugel, R. Majeski, J. Timberlake, Low recycling regime in ITER and the LiWall concept for its divertor. J. Nucl. Mater. **363–365**(1–3), 453–457 (2007). https://doi.org/10.1016/j.jnucmat.2007.01.230
78. T. Pütterich, E. Fable, R. Dux, M. O'Mullane, R. Neu, M. Siccinio, Determination of the tolerable impurity concentrations in a fusion reactor using a consistent set of cooling factors. Nucl. Fusion **59**(5), 056013 (2019). https://doi.org/10.1088/1741-4326/ab0384
79. J. Rodríguez-Rodríguez, A. Casado-Chacón, D. Fuster, Physics of beer tapping. Phys. Rev. Lett. **113**(21), 1–5 (2014). https://doi.org/10.1103/PhysRevLett.113.214501. arXiv:1403.2678
80. R.J. Goldston, A. Hakim, G.W. Hammett, M.A. Jaworski, J. Schwartz, Recent advances towards a lithium vapor box divertor. Nucl. Mater. Energy **12**, 1118–1121 (2017). https://doi.org/10.1016/j.nme.2017.03.020
81. P.M. Valanju, M. Kotschenreuther, S.M. Mahajan, Super X divertors for solving heat and neutron flux problems of fusion devices. Fusion Eng. Des. **85**(1), 46–52 (2010). https://doi.org/10.1016/j.fusengdes.2009.06.001
82. G. Fishpool, J. Canik, G. Cunningham, J. Harrison, I. Katramados, A. Kirk, M. Kovari, H. Meyer, R. Scannell, MAST-upgrade divertor facility and assessing performance of long-legged divertors. J. Nucl. Mater. **438**(SUPPL), S356–S359 (2013). https://doi.org/10.1016/j.jnucmat.2013.01.067
83. T. Tanabe, Tritium issues to be solved for establishment of a fusion reactor. Fusion Eng. Des. **87**(5–6), 722–727 (2012). https://doi.org/10.1016/j.fusengdes.2012.02.009
84. M. Christenson, C. Moynihan, D.N. Ruzic, A distillation column for hydrogen isotope removal from liquid lithium. Fusion Eng. Des. **135**, 81–87 (2018). https://doi.org/10.1016/j.fusengdes.2018.07.009
85. S.A. Krat, A.S. Popkov, Y.A. Vasina, Y.M. Gasparyan, A.A. Pisarev, Lithium-deuterium co-deposition. J. Nucl. Mater. **584**, 154598 (2023) https://doi.org/10.1016/j.jnucmat.2023.154598
86. J.W. Coenen, G. De Temmerman, G. Federici, V. Philipps, G. Sergienko, G. Strohmayer, A. Terra, B. Unterberg, T. Wegener, D.C. Van Den Bekerom, Liquid metals as alternative solution for the power exhaust of future fusion devices: status and perspective. Phys. Scr. (2014). https://doi.org/10.1088/0031-8949/2014/T159/014037
87. C.E. Kessel, D. Andruczyk, J.P. Blanchard, T. Bohm, A. Davis, K. Hollis, P.W. Humrickhouse, M. Hvasta, M. Jaworski, J. Jun, Y. Katoh, A. Khodak, J. Klein, E. Kolemen, G. Larsen, R. Majeski, B.J. Merrill, N.B. Morley, G.H. Neilson, B. Pint, M.E. Rensink, T.D. Rognlien, A.F. Rowcliffe, S. Smolentsev, M.S. Tillack, L.M. Waganer, G.M. Wallace, P. Wilson, S.J. Yoon, Critical exploration of liquid metal plasma-facing components in a fusion nuclear science facility. Fusion Sci. Technol. **75**(8), 886–917 (2019). https://doi.org/10.1080/15361055.2019.1610685
88. F. Barbier, J. Blanc, Corrosion of martensitic and austenitic steels in liquid gallium. J. Mater. Res. **14**(3), 737–744 (1999). https://doi.org/10.1557/JMR.1999.0099
89. M. Kondo, M. Ishii, T. Muroga, Corrosion of steels in molten gallium (Ga), tin (Sn) and tin lithium alloy (Sn-20Li). Fusion Eng. Des. **98–99**, 2003–2008 (2015). https://doi.org/10.1016/j.fusengdes.2015.05.051
90. S.J. Zinkle, ORNL, Summary of Physical Properties for Lithium, Pb-17Li, and (LiF)n·BeF2 Coolants, Technical report (1998). https://bpb-us-w2.wpmucdn.com/research.seas.ucla.edu/dist/d/39/files/2019/08/1zinkle0798.pdf. Accessed 22 Feb 2023
91. S. Hardy, The surface tension of liquid gallium. J. Cryst. Growth **71**(3), 602–606 (1985). https://doi.org/10.1016/0022-0248(85)90367-7
92. M.J. Assael, I.J. Armyra, J. Brillo, S.V. Stankus, J. Wu, W.A. Wakeham, Reference data for the density and viscosity of liquid cadmium, cobalt, gallium, indium, mercury, silicon, thallium, and zinc. J. Phys. Chem. Ref. Data (2012). https://doi.org/10.1063/1.4729873
93. B.B. Alchagirov, R.K. Dadashev, F.F. Dyshekova, D.Z. Elimkhanov, Temperature dependence of the surface tension of indium. Russ. J. Phys. Chem. A **87**(6), 890–894 (2013). https://doi.org/10.1134/S0036024413050026
94. A. Passerone, R. Sangiorgi, G. Caracciolo, The surface tension of liquid lead. J. Chem. Thermodyn. **15**(10), 971–983 (1983). https://doi.org/10.1016/0021-9614(83)90131-3
95. F.A. Kanda, R.P. Colburn, The absolute viscosity of some lead-tin alloys. Phys. Chem. Liq. **1**(2), 159–170 (1968). https://doi.org/10.1080/00319106808083795
96. A.E. Schwaneke, W.L. Falke, Surface tension and density of liquid lead. J. Chem. Eng. Data **17**(3), 291–293 (1972). https://doi.org/10.1021/je60054a016
97. W. Gasior, J. Pstruś, Z. Moser, A. Krzyzak, K. Fitzner, Surface tension and thermodynamic properties of liquid Ag–Bi solutions. J. Phase Equilib. **24**(1), 40–49 (2003). https://doi.org/10.1361/105497103770330983
98. Y. Plevachuk, V. Sklyarchuk, G. Gerbeth, S. Eckert, Thermophysical properties of liquid tin-bismuth alloys. Int. J. Mater. Res. **101**(7), 839–844 (2010). https://doi.org/10.3139/146.110357
99. J. Cahill, A. Kirshenbaum, The density of liquid bismuth from its melting point to its normal boiling point and an estimate of its critical constants. J. Inorg. Nucl. Chem. **25**(5), 501–506 (1963). https://doi.org/10.1016/0022-1902(63)80233-X